ABSTRACT

Title of Thesis: FABRICATION AND MEASUREMENT OF CESIATED METAL PHOTOCATHODES

Nathan A. Moody, Master of Science, 2004

Thesis Directed By: Professor Patrick O'Shea
Department of Electrical and Computer Engineering

A requirement for accelerator applications such as free electron lasers is a high current, high quality electron beam. This is achieved using a photoinjector, where a drive laser modulates the electron emission of a cathode in the presence of an electric field. Current photocathodes are plagued with limited efficiency and short lifetime, due to contamination or evaporation of a photosensitive surface layer. An ideal photocathode would have high efficiency in the visible range, long lifetime, and prompt emission. Cathodes with high efficiency typically have limited lifetime, and vice versa. A potential solution is the dispenser cathode, where limited lifetime is overcome by periodic *in situ* regeneration that restores the photosensitive surface. This project prepares for fabrication of dispenser cathodes by studying the properties of cesiated tungsten. A test facility was constructed and used to fabricate and test cesiated tungsten cathodes, whose behavior closely agreed with recently developed photoemission theory at the Naval Research Laboratory.

FABRICATION AND MEASUREMENT OF CESIATED METAL PHOTOCATHODES

by

Nathan Moody

Thesis submitted to the Faculty of the Graduate School of the University of Maryland, College Park, in partial fulfillment of the requirements for the degree of Master of Science
2004

Advisory Committee:

Professor Patrick G. O'Shea, Chair/Advisor
Professor Isaak D. Mayergoyz
Professor John Melngailis

Dedication

To my wife.

Acknowledgements

My experience in graduate school thus far has been a fruitful and rewarding one due in large part to the time and effort of many individuals. Professor O'Shea is first among this group because he saw in me the potential to do research and succeed in graduate school and expressed that belief by offering me a GRA. The discussions with him have shaped my outlook and approach to graduate school and I can only aspire to be such an influence in someone else's life one day. Dr. Don and Renee Feldman were the first to welcome me as a graduate student and I am very grateful for the countless discussions we have had that helped define the direction of the cathode research program, among many other things. Dr. Kevin Jensen has lent enormous help by explaining his theories and that of many others in ways I can understand. His work lends significance and credibility to this project.

Beyond his much appreciated help in experimental techniques, Bryan Quinn has been an excellent friend since our undergraduate days and (I believe) played a significant role in helping me get hired. IREAP is an ideal environment in which to work because of the large pool of talented people who have a warm disposition toward graduate students and a willingness to answer questions or lend a helping hand. I would like to thank Nolan Ballew, Jay Pyle, Dr. John Rodgers, Dr. Mark Walter, Doug Cohen, and Bart Hogan for their support and expert advice in helping me set up my experiment. I would also like to thank past and present graduate students Matt Virgo, Jonathan Neumann, John Harris, Todd Firestone, David Demske, Yijie Huo, Roland Ngogang, Gang Bai, and Oleks Sinitsyn for their support, friendship, and advice along the way.

I wish also to thank Professor J. Melngailis and Professor I. Mayergoyz for serving on my thesis exam committee. Furthermore, I am especially thankful to Professor Mayergoyz for allowing me to learn alongside him as he taught his exemplary quantum mechanics course and shared valuable insights, both personal and academic in nature.

Support for this research program comes from the Joint Technology Office (JTO) and the Office of Naval Research (ONR) and it is gratefully acknowledged.

I would also like to thank my parents for their lifelong example and unwavering support in all my endeavors, academic or otherwise.

And most of all, I must express immeasurable gratitude to my wife and best friend Daniela for putting up with all that goes along with graduate school and for valuing and supporting my dreams.

Table of Contents

List of Tables

List of Figures

Chapter 1: Introduction

1.1 Overview

Photocathodes have been used for decades in radiation detectors and imaging tubes [1], but only recently have become a source for high brightness electron beams [2]. In such applications, a photocathode is illuminated by a short laser pulse and the ejected electrons are subjected to the accelerating gradient of a synchronized RF field. A photocathode-based accelerator source is referred to as a photoinjector, the first of which was developed at SLAC as a sourced of polarized electrons for particle physics experiments.

The great advantage of using a photoinjector is the ability to modulate the electron beam using a relatively simple drive laser. The beam is then rapidly accelerated to relativistic energies, preserving its initial shape and quality. An important characteristic of a photocathode is its quantum efficiency (QE) – the ratio of emitted electrons to incident photons. Techniques for improving this figure are a main topic of this project.

Traditional thermionic injectors, while simple and robust, are not capable of producing beams of the requisite quality for many applications, such as free electron lasers. In thermionic emission, a heated cathode emits low energy electrons in a gated field which are then longitudinally compressed in sub-harmonic bunching cavities prior to being accelerated to relativistic energies. This compression process degrades the initial beam quality because nonlinear forces from space-charge and bunching fields lead to emittance growth [3]. A photoinjector avoids this difficultly altogether by producing the desired pulse shape directly at the cathode.

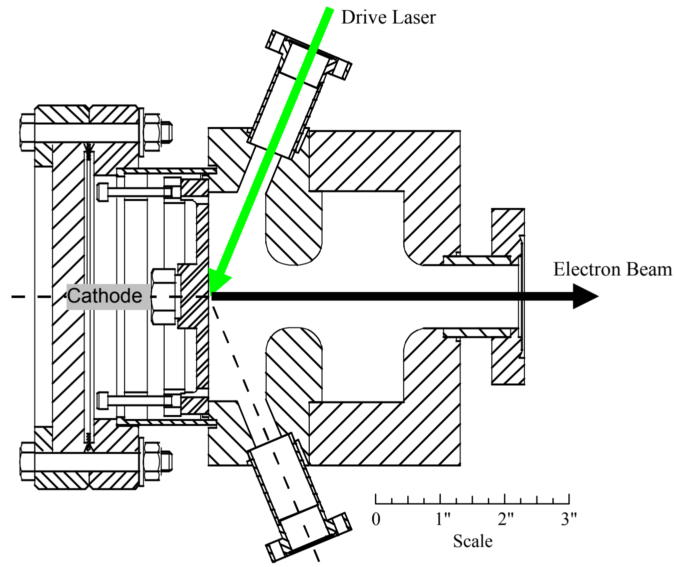

Figure 1: Schematic of photoinjector

The quest has been to find the optimum photocathode for use in a practical photoinjector. An ideal photocathode should have high quantum efficiency (QE), fast temporal response, long lifetime, and minimal complexity [4]. Such cathodes do not currently exist, and the accelerator community has struggled to find compromises among these factors. In order to preserve practical drive laser requirements, a fast photocathode with good quantum efficiency (>1%) in the visible or soft ultraviolet is desired. Metal photocathodes such as copper exhibit long lifetime and fast response, but have quite low quantum efficiency ($<10^{-4}$) due to their high optical reflectivity and high workfunction. Semiconductor photocathodes have much better QE (on the order of several percent) but are slow emitters and last less than a day in practical vacuum situations $(\sim 10^{-9})$ [4]. Lifetime is limited for various reasons, depending on whether the cathode is metallic or semiconductor in nature, and depends on the background pressure of the system.

This project focuses on understanding the photoemission process of cesiated tungsten as a starting point for designing more complex cathode systems. Cesium and other alkali metals are known to reduce the workfunction of the substrate onto which they are evaporated. Qualitatively, this is due to the fact that the cesium atoms give up their single valence electron and reside on the surface as a positive charge. The effective dipole moment set up by these charges at the surface assists the electron in crossing the barrier potential, leading to a lowered workfunction. The reduction in workfunction is sufficient to allow some metals to perform reasonably well as photoemitters in the green and blue regions of the optical spectrum. Desorption (and chemical reactivity) of the photosensitive cesium layer, however, causes QE to decrease with time because the layer is both leaving the surface and being poisoned by contaminates. If this layer could be replenished *in situ*, then lifetime would be less of a problem because a short rejuvenation period could restore the cathode's photosensitive layer. Such a cathode is termed a *dispenser* cathode. A theory to account for the process of photoemission from cesiated metals has been developed at the Naval Research Laboratory [5]. In a collaborative effort with NRL, this theory has been compared with experimental results and found to agree exceedingly well. Therefore, experimental methods outlined in this project, together with the NRL theory, provide a sound starting point for the development of alkali-metal dispenser cathode systems.

1.2 Historical Background

The photoelectric effect was discovered in 1887 by Hertz when he observed that the distance across which a spark could be induced was increased when ultraviolet light irradiated the negative electrode [6]. Hallwachs observed the same effect by discharging negatively charged zinc electrodes with ultraviolet light (he observed that positively charged electrodes could not be discharged in this manner). Elster and Geitel then discovered in 1889 that visible light could produce noticeable photoelectric effects in alkali metals [7]. After J. J. Thomson discovered the electron in 1899, the photoelectric effect could be understood as electron emission induced by electromagnetic radiation.

Measurements showed that photocurrent was linearly proportional to light intensity and electron energy was proportional to frequency. These relationships could not be explained via classical electromagnetic theory (which would predict that increased intensity would lead to increasingly energetic photoelectrons). Einstein's response in 1905 was that this is a quantum mechanical effect where photons impinging upon a surface are converted to free electrons, earning him the Nobel Prize of 1921. The photoelectric effect, because of its contradiction with classical theory, played a central role in the development of modern quantum mechanics. Einstein stated that given incident light with frequency ν, the maximum kinetic energy of an ejected electron is given by:

$$\frac{1}{2}mv^2 = h\nu - \phi \tag{1.1}$$

where ϕ is the workfunction of the material (i.e. the work that must be done to liberate an electron). The energy of emitted electrons can be determined by measuring the stopping potential V_s required to bring them to rest:

$$V_s q = \frac{1}{2} m v^2 \tag{1.2}$$

Much of the work following Einstein was designed more to establish a body of evidence for quantum theory than to actually expand photocathode technology. Photocathodes during this period were mostly metallic and had very low quantum efficiencies. It was not until the discovery of the “silver-oxygen-cesium” cathode in 1929 that interest in photoemission shifted from pure research to practical application [8],[9]. Other complex photosensitive materials besides Ag-O-Cs were discovered during the next decade through a process of intelligent guessing, but the specific mechanism of photoemission in these materials was not understood until much later.

During the 1940’s, the emphasis shifted toward explaining photoemission in terms of fundamental concepts and led to the realization that most promising photosensitive compounds were semiconductors. As solid state physics grew rapidly through the 40’s, 50’s, and ‘60’s, the concept of negative electron affinity (NEA) surfaced and led to cathodes that outperformed those discovered empirically, at least in terms of quantum efficiency.

1.3 Theory of Photoemission

The process of photoemission can be viewed as a three-step process consisting of 1.) photon absorption, 2.) electron migration to the surface, and 3.) overcoming the barrier potential [10]. This perspective allows photoemission to be related to characteristics of the material, such as scattering coefficient, optical reflectivity, and potential barrier height. Using this theory, the response times of existing cathodes can be estimated and are found to cover a range of six orders of magnitude [11]. In general, there is an inverse relationship between the response time of a photocathode and its quantum efficiency.

Metals make very prompt emitters because electrons which can escape the barrier are found very close to the surface, but the high optical reflectivity of metals greatly limits their quantum efficiency because few photons are actually absorbed. Semiconductors, however, are less reflective and less conductive, so more photons are absorbed and are capable of escaping upon arriving at the surface. Because more electrons can overcome the surface barrier in semiconductors, they tend to have higher quantum efficiencies than metals. Since many electrons come from within the bulk, however, their transit time to the surface lengthens the response time. For accelerator applications, a fast temporal response is required so that the electron pulse occupies only a small fraction of the RF phase. If this is not the case, then electrons throughout the bunch experience different accelerating gradients and end up having a spread of energies.

During the first fifty years of study on photoemission, it was considered a surface, rather than bulk effect [11]. But the first monolayer can absorb at best 10% of the incoming light [13] and if this were to account for the entire process, the quantum efficiency could not exceed 0.001 for any material [1]. This is clearly not the case, so photoemission in general must be considered an event involving both the surface and the bulk. In modern literature, the term 'surface' is reserved for the literal monomolecular layer of a material. A primary distinction between the various types of photocathodes is the degree to which they can be considered metallic versus semiconducting. It is useful to distinguish between these two cases. Using band theory, metals are distinguished from insulators and semiconductors by the fact that, at absolute zero, their conduction band remains partially full. Semiconductors, at absolute zero, will have an empty conduction band separated by gap E_g from a full valence band. Thus, ideal semiconductors are perfect insulators at absolute zero, but as temperature is increased some electrons are promoted to the conduction band giving rise to conductivity. In context of photoemission, in order for an electron to escape to vacuum, it must overcome not only the band gap but also the surface potential barrier, given by the electron affinity E_A.

1.3.1 Spicer's Three Step Model

Step one in Spicer's three step model is photon absorption. Because of the characteristically high optical reflectivity in metals, the process of photon absorption is inherently limited. Semiconductors are less reflective than metals and consequently more incident photons are absorbed if their energy exceeds the bandgap [10].

Step two involves the process by which a photoelectron travels to the surface. An electron which has absorbed a photon is considered a *hot* electron because its energy is higher than that of other electrons in thermal equilibrium. Any interactions between this photoelectron and other electrons or the lattice will reduce the chances of it arriving at the surface with sufficient energy to cross the barrier. Because of the abundance of free electrons in metals, a photoelectron will undergo many collisions with other electrons and rapidly thermalize. Only electrons excited within a few atomic layers of the surface will arrive with sufficient energy to escape and contribute to photoemission. In semiconductors, the dominant scattering mechanism is electron-phonon interaction. The energy loss per lattice interaction is much less than the energy loss per electron-electron interaction, so photoelectrons in semiconductors can travel much further distances (compared to electrons in a metal) before reaching thermal equilibrium. This means that for a given number of incident photons, more photoelectrons will reach the surface with sufficient energy to cross the barrier potential.

The third step in Spicer's model involves the surface barrier. For metals, the surface barrier is simply the workfunction. Photoelectrons excited within the metal can only escape to vacuum if their energy upon arrival at the surface exceeds the workfunction. The workfunction of most metals is rather high, as seen in Table 1.

Metal	ϕ (eV)
Silver	4.26
Copper	4.65
Molybdenum	4.37
Tungsten	4.65
Cesium	2.14

Table 1 Workfunctions of Various Metals.

As stated before, a photoelectron in a semiconductor can only cross the surface barrier if it has energy equal to $E_A + E_g$. From this discussion it is obvious that metals will have much lower quantum efficiencies than semiconductors, but will have faster response times.

Because metal cathodes can tolerate high electric fields, an effect analogous to the Schottky effect in thermionic emission can be used to effectively reduce the workfunction and improve quantum efficiency. In RF guns, fields on the order of 50 MeV/m can be achieved. This can reduce the amount of energy needed by a photoelectron to escape to the vacuum, causing a shift in the threshold wavelength toward the red. It was found that the magnitude of the shift is roughly proportional to the square root of the applied field [11].

1.4 Characteristics of Photocathodes

The relevant properties that characterize a photocathode are spectral response, operational lifetime, temporal response, damage threshold, and transverse energy spread (of emitted electrons). Each of these is discussed in turn.

1.4.1 Spectral Response

Spectral response refers to the manner in which quantum efficiency varies with the frequency of incident light. Some photocathodes may operate over an entire range of frequencies, while others perform best in the UV, for example. Copper and cesium telluride respond only to ultraviolet, while potassium cesium antimonide and cesiated metals can be operated in the visible spectrum. The best photoemitters have quantum efficiencies approaching 50%, while typical values range from 0.001-10%. The wide variation in quantum efficiencies is due to the events that occur as the electron migrates to the surface of a photocathode, as discussed in the previous section. The threshold wavelength corresponds to the lowest frequency of incoming light with sufficient energy to overcome either the workfunction (in a metal) or the bandgap plus the electron affinity (in a semiconductor), as shown in Figure 2.

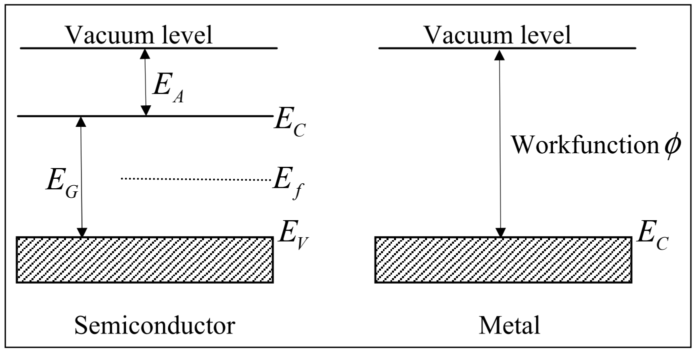

Figure 2: Band structure for semiconductors and metals

1.4.2 Lifetime

The operational lifetime of a photocathode depends largely on the vacuum in which it operates. Several factors may contribute to limited lifetime, depending on the type of cathode in question. For semiconductors, adsorbed surface films and surface oxides tend to decrease quantum efficiency. The rate at which these films form depends on the background pressure and composition. Ion back bombardment in DC guns damages the cathode surface and degrades performance. For alkali-metal systems such as cesiated tungsten, the photosensitive layer can desorb because of localized heating or be damaged by the mechanisms described above. Certain compounds such as water and carbon monoxide can “poison” the cathode, further reducing its operational lifetime. Dispenser cathodes have an extended operational lifetime because their photosensitive surface films can be rejuvenated to some extent during a periodic reconditioning period.

1.4.3 Response time

The response time of a photocathode depends upon the penetration depth of incident photons. If photoelectrons are created deep within the bulk and have sufficient energy to escape to vacuum upon arriving at the surface, then their transit time determines the promptness of emission. Because the penetration depth for photons in metals is shallow, photoelectrons are created only very near the surface. Because they have only a miniscule distance to travel to the surface, they result in prompt emission and can closely follow the short pulses (picoseconds) of a drive laser.

1.4.4 Damage Threshold

Damage threshold refers to the maximum laser intensity a photocathode can withstand without suffering damage to its surface. Cathodes that utilize surface films to reduce workfunction are more delicate and will have lower damage thresholds than bare metals. The damage mechanisms are usually localized heating or plasma formation at the surface. Damage threshold is not considered a critical cathode parameter because the intensity of most drive lasers is well beneath it.

1.4.5 Transverse Energy Spread

Cathodes with low workfunctions permit the generation of photoelectrons with energies well above that required to escape to vacuum. Consequently, some of these can suffer collisions and still escape, although with lower energy than those that do not suffer collision. Because emitted electrons have a range of energies, a transverse energy spread is imparted to the resulting beam. The variation, however, is on the order of an electron volt, so when the beam is accelerated to much higher energies these small differences become less important. Only in applications with low beam energy is transverse energy spread of the emitted electrons considered critical.

Characteristics of some commonly used cathodes, including metals and semiconductors, are listed in Table 2.

Material	λ (nm)	QE at λ	Lifetime	Response Time	Vacuum (Torr)	Max Field (MV/m)
Cs_3Sb	527	4%	$T_{1/2} < 4$ h	~1 ps	10^{-9}	> 20
Cs_2Te	263	13%	$T_{1/e} > 100$ h	~3 ps	10^{-9}	> 20
K_2CsSb	527	8%	$T_{1/2} < 4$ h	~1 ps	10^{-9}	> 20
Cu	266	1.4×10^{-4}	very long	< ps	10^{-7}	> 100
Y	266	5×10^{-4}	long	< ps	$< 10^{-7}$	~100
Mg	266	6×10^{-4}	> 5000 h	< ps	10^{-7}	~20
Ba	337	0.1%	2 hr	< ps	$< 10^{-7}$	~50

Table 2: Characteristics of various photocathodes

1.5 Measuring Workfunction

The workfunction is a fundamental characteristic of metallic cathodes and various experimental methods are employed to measure it. There are three ways generally used: thermionic emission, photoemission, and contact potential difference.

1.5.1 Thermionic Emission

The energy required for an electron to escape to vacuum from a metal surface can be obtained by making use of the Richardson equation:

$$I = AT^2 e^{\frac{-e\phi}{k_B T}} \tag{1.3}$$

where T is the temperature, I is the current. If I/T^2 is plotted versus $1/T$, the resulting straight line is called the Richardson line [11] and its slope is ϕ.

1.5.2 Photoemission Measurements

Fowler developed a theory in the 1930's that predicts the shape of spectral response curves in the threshold region [14], a so-called Fowler plot. By fitting such a plot to an experimental curve, an exact value for workfunction can be obtained. DuBridge extended this method such that the wavelength of incident light could be held constant and the cathode temperature varied instead. The workfunction can then be found by measuring the quantum efficiency as a function of temperature. A third way to utilize photoemission to determine workfunction is to measure the maximum velocity of emitted electrons using a retarding field and monochromatic light [15].

1.5.3 Contact Potential Difference

If two metals with different workfunctions are brought into contact, electrons from the lower workfunction metal will migrate to the higher workfunction metal, leaving the first metal positive and the other negative. This gives rise to a potential difference at the contact surface equal to the difference of the workfunctions. Therefore, if the workfunction of one metal is reliably known, that of another can be found by measuring this contact potential difference (CPD). A common arrangement is to direct an electron beam onto both a reference metal and one whose workfunction is to be determined. If the current from each electrode is plotted with respect to the voltage, the two curves are displaced relative to each other by an amount equal to the difference of workfunctions [16]. Although this method seems experimentally simple, contamination of the reference metal can easily lead to erroneous results. And because the thermionic method is useful only for metals with sufficiently high melting points, the Fowler method is the most universally applicable method of measuring the workfunction of a metal.

1.6 Effect of Surface Films on Workfunction

Surface films can greatly alter the photoemissive properties of a material and can be used to fabricate more efficient photocathodes. The effect of a surface film on the workfunction of a material depends upon the film composition and upon the bonding mechanism involved. If the binding forces between the substrate and the film are weak (i.e. Van der Waals bonds), then the effect of this film on the workfunction is negligibly small [15]. Conversely, if there is a strong ionic character to the bond, the resulting dipoles at the surface, depending on their polarity, either increase or decrease the workfunction.

The precise relationship between the thickness of a surface film and the workfunction of the substrate is very complicated and is a focal point of the research at NRL [17]. It is widely observed that the thicknesses of interest to the properties of photoemission are on the order of monolayers (usually less than a monolayer). This is because the emission process occurs within a few hundred Ångstroms of the surface barrier. If the surface film were to have this same thickness, then the emission properties observed would be those of the film itself, not of the substrate. Because this project involves metallic cathodes, the discussion of surface films assumes a metallic substrate.

1.6.1 Non-metallic Surface Films

Except for the noble gases, some degree of ionic bonding will always occur between the metal and a surface layer. Adsorbed layers of argon, for example, have little or no effect on the metal's workfunction because a surface dipole moment is not created. Elements on the right hand side of the periodic table are electronegative and as a surface film increase the workfunction of the metal. The opposite is true of films formed from elements on the left of the periodic table: the positive charge assists the escape of electrons from the surface and reduces the workfunction. Surface films of oxygen on metals, for example, will increase the workfunction unless the resulting oxide diffuses into the bulk and exposes new atomic layers of the metal [18].

1.6.2 Metallic Surface Films

Because alkali and alkali-earth metals form dipoles on the surface of metals that facilitate photoemission, they are the most effective at reducing the workfunction. This effect was observed by Langmuir [19] in his studies on the thermionic emission of tungsten in a cesium vapor. He found that for a cesium surface layer on tungsten, the resulting workfunction of the two materials was lower than either of them taken individually. Subsequent experimentation has lead to much controversy over the years as to what amount of cesium (or other alkali metal) is optimal for workfunction reduction. It appears the experiments of Langmuir and others, including this project, suggest that the workfunction reduction is greatest for *less* than a monolayer of adsorbed cesium. The question becomes the definition of what constitutes a monolayer (i.e. how many atoms are associated with a monolayer). Even if a surface density of atoms is assumed or calculated, the microscopic surface area is difficult to determine for all but single crystals because polycrystalline metals are microscopically irregular. In any case, Langmuir published an optimal coverage factor of Cs on W at about 70%, which agrees with more recent work as well as the experiment described in the next chapter.

In addition to an optimal coverage, another factor is directly correlated to the workfunction: the *difference* between ionization energy of the alkali metal and the workfunction of the substrate. If this difference is augmented, the workfunction is reduced. Minimum workfunction values for Cs-W vary from 1.4 – 1.7 eV. Notice that Cs has ionization energy of 3.87 eV, while W has a workfunction of 4.65 eV. The difference between the two (0.78 eV) is greater, for example, than the corresponding difference for the case of K and W. Consequently, a surface layer of potassium has less of a workfunction reduction effect on tungsten than cesium does. Other ionization energies are listed in Table 3.

Metal	Ionization Energy (eV)
Ba	5.19
Ca	6.09
Cs	3.87
K	4.16
Na	5.12

Table 3: Ionization energies for selected alkali metals

It is also reported that for single crystals, the extent to which the workfunction is reduced depends upon which crystal face the alkali film is formed [15]. On single crystals of tungsten, for example, the (100) face has a lower workfunction at $\phi = 1.82\text{eV}$ than the (110) face with $\phi = 2.06\text{eV}$ [20]. Lastly, it is important to realize that because cesium is so electropositive, it will have a workfunction-reducing effect on many metals. In the case of copper, cesium reduces the workfunction from 4.54 eV to 1.55 eV and for silver the reduction is from 4.62 eV to 1.55 eV [11].

1.6 Project Summary

This project details the following accomplishments:

- Design and construction of a UHV cathode preparation chamber
- Computer integration of instrumentation for data acquisition
- Reproducible fabrication of cesiated tungsten photocathodes
- Measurement of photocurrent to determine quantum efficiency (QE)
- Close agreement of QE data to recently developed theory
- Design and fabrication of prototype dispenser photocathode

This thesis is organized as follows:

- Chapter 2: experimental setup
- Chapter 3: experimental results
- Chapter 4: analysis / interpretation of data, comparison to theory
- Chapter 5: Concluding discussions

Chapter 2: Experimental Setup

2.1 Test Chamber

Evaporation and deposition of photosensitive materials must be performed in ultra-high vacuum. The UHV system is built around an electropolished four-way cross with 8" flange plates that facilitate a versatile arrangement of feedthroughs, optical windows, diagnostics, and pumping ports. The cross is anchored to a large bench breadboard via an aluminum chassis, all of which are electrically strapped to ground potential.

2.1.1 Test Chamber Geometry

The vacuum is maintained by a 200 liter/sec ion pump situated at the bottom 8" port (labeled *A* in Figure 3) and is assisted by a smaller 40 liter/sec ion pump at the top of the chamber (port *B*). A residual gas analyzer (RGA), ion gauge, and deposition monitor also are connected to the top plate using standard CF 2.75" hardware.

The front plate *C* houses the cesium evaporation sources and has viewports for the laser as well as high-current feedthroughs that allow a current to be passed through the sources during activation. The cathode assembly is connected to plate *D* along with a thermocouple gauge and fine metering value used to introduce trace gases into the vacuum. Each of these components are discussed individually elsewhere and shown assembled in Figure 4.

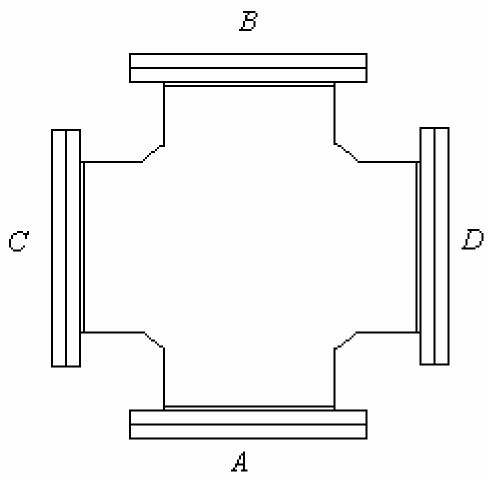

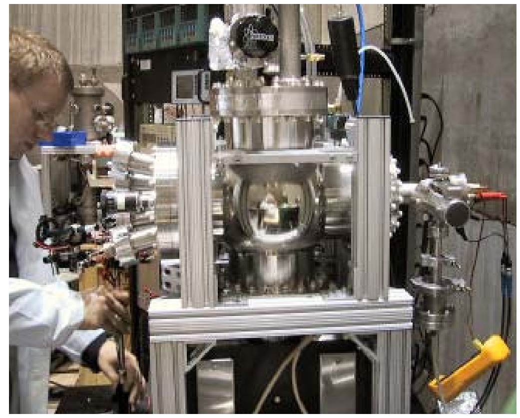

Figure 3: Four way cross in UHV system

Figure 4: Installed four way cross

Attached to the inner side of plate *C* are three cesium evaporation sources (from SAES, Italy) which consist of a nichrome metal envelope 12mm in length containing cesium chromate and a reducing agent. When sufficient current is passed through the nichrome enclosure, cesium atoms are released from a slit along the top at a controlled rate. These sources and their current leads are shown in Figure 5. To abruptly halt evaporation, a shutter mask is placed over the source as in Figure 6.

Figure 5 Cesium dispensers

Figure 6: Shutter mask for cesium dispensers

During the evaporation stage, the quantum efficiency is monitored by shining a laser onto the cathode in the presence of an electric field while measuring the resulting photocurrent as a function of evaporated thickness or coverage. The laser and observation viewports are located also on plate *C*, the exterior of which is shown in Figure 7.

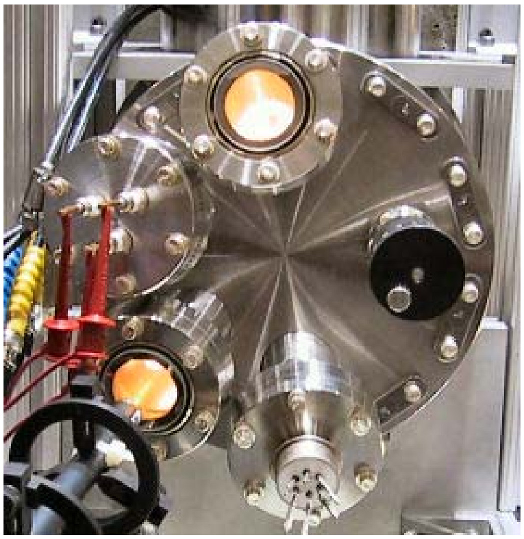

Figure 7: Exterior of plate *C*

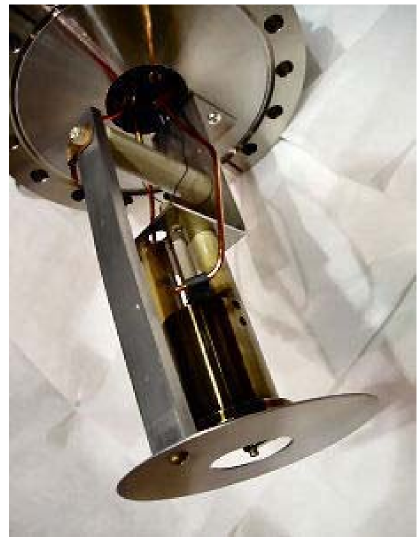

Figure 8: Cathode assembly on plate *D*

Figure 8 illustrates the cathode assembly which is mounted opposite the evaporation sources at plate *D*. The annular disk at the bottom of the figure is the anode, which serves a dual purpose in the present configuration. Besides collecting photocurrent, the anode serves as a shadow mask to shield other vacuum components from undesired cesium deposition. The cathode, consisting of a thin tungsten disk 1" in diameter, is mounted on a button heater 1 cm behind the anode. The heater is mounted within a heat shield assembly, shown in Figure 9, which accommodates a thermocouple to monitor cathode temperature.

The anode and cathode are kept electrically isolated from each other and the chamber by a set of ceramic standoffs that also provide mechanical support, as shown in Figure 10. The entire anode/cathode assembly, shown head-on in Figure 11, is situated such that the cathode is directly in the center of the four-way cross.

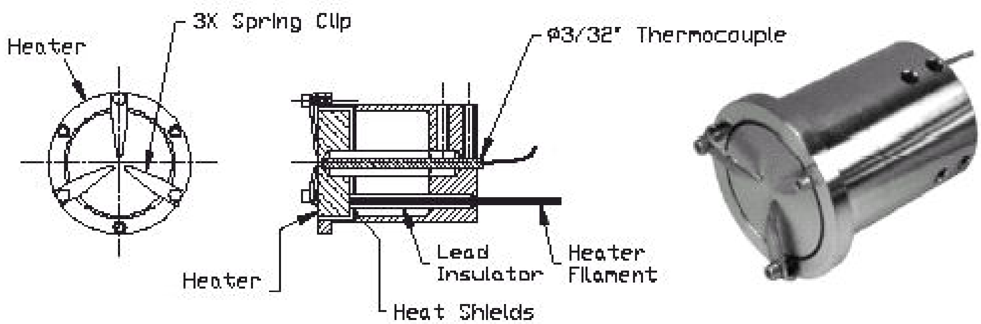

Figure 9 Cathode heater geometry.

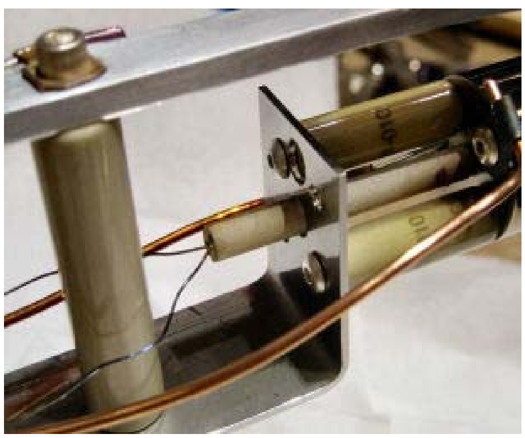

Figure 10: Electrical standoffs

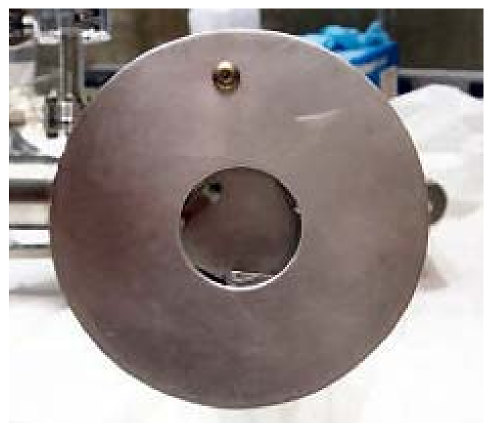

Figure 11: Front view of anode/cathode

2.1.2 Vacuum Procedures

Photoemission measurements require ultra-high vacuum primarily because the cathode surface is vulnerable to contamination during evaporation and measurement stages. Standard vacuum procedures for handling components were followed to prevent contamination and a bakeout schedule was used during each pumping period. Figure 12 shows a calculated pressure profile along the vertical axis of the test chamber, where the origin corresponds to the upper ion pump and the distance 0.7m corresponds to the lower end of the bottom pump.

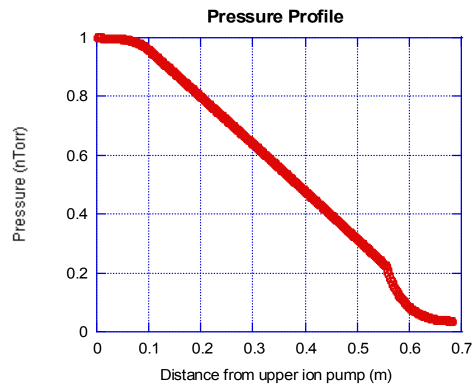

Figure 12: Pressure profile within vacuum chamber

The calculation was performed using a vacuum simulation program developed at SLAC called VACCALC, which solves the differential equations relating pressure P, conductance c, pumping speed s, and outgas rate q , using a piecewise method [21]. The differential equation relating these quantities is:

$$c\frac{d^2P}{dz^2} - sP + q = 0 \tag{1.4}$$

Solutions to this equation are given by:

$$P(z) = C_1 e^{\alpha z} + C_2 e^{-\alpha z} + \frac{q}{c} \tag{1.5}$$

which are valid only if the conductance c is constant. Because the chamber geometry varies with position, however, the conductance also will vary with position. For this reason, VACCALC uses a method of finite differences and considers c to be constant over each segment [22]. The simulation inputs are the chamber geometry, temperature, and pumping speeds and the output is pressure as a function of position in the vacuum system. The calculated pressures match the observed pressures after sufficient baking, so the assumption was made that the pressure at the cathode (at room temperature) is about 5×10^{-10} Torr.

A crucial step in preparing for cesium evaporation is the out-gassing of the cesium sources. This is achieved by passing a mild current through the source while monitoring change in pressure. For new sources, the outgassing rate is beyond what can be sustained by ion pumping, so some outgassing is performed during rough pumping to minimize the gas load.

The term ‘bakeout’ refers to heating the chamber and all vacuum components to $>200^{\circ}\mathrm{C}$ during pumping periods in an effort to accelerate the desorption of gas molecules that stick to surfaces. If this step is not performed, gas molecules will leave the surface at a slow rate over a long period of time, giving rise to a rather high background pressure (mimicking a slow leak). Thus, bakeouts are crucial to achieving a good vacuum in a reasonable amount of time.

It was determined that approximated 14 hours of rough pumping were required to bring the system from atmospheric pressure down to about 1×10^{-6} Torr, the pressure at which ion pumps can be used. During bakeout, aluminum foil is wrapped around the entire chamber to prevent convection and permit higher bakeout temperatures (up to $260^{\circ}\mathrm{C}$). After roughing pressure is attained and the ion pumps are turned on, another 24 hours of bakeout and pumping are required to achieve a pressure of $\sim 5\times10^{-8}$ Torr. After a cool-down period, the system is ready for use. In order to prevent contaminants from leaving the chamber walls and adhering to the cathode surface, the cathode is kept at a higher temperature than the rest of the system during bakeout and source degassing. The only major deviations from these procedures are when new components are introduced into the system or after the system is flushed with argon. Because argon is chemically inert, it is pumped much more slowly by the ion pumps than other gases and so longer pumping and bakeout periods are required to achieve target pressures after argon use.

2.2 Electronics

The instrumentation scheme of this experiment is designed for automated data acquisition via Labview. A GBIP controller communicates with 8 instruments over a common GPIB signaling bus to send commands and receive data at specific intervals during an experimental measurement. Custom drivers for each instrument were written in Labview to accommodate device specific commands and operations. Data received from the instruments is time-stamped and saved to disk in real time for later analysis using the scheme diagramed in Figure 13. The polling period for most experiments is set to 300ms, to provide sufficient time resolution of measurements such as photocurrent and quantum efficiency.

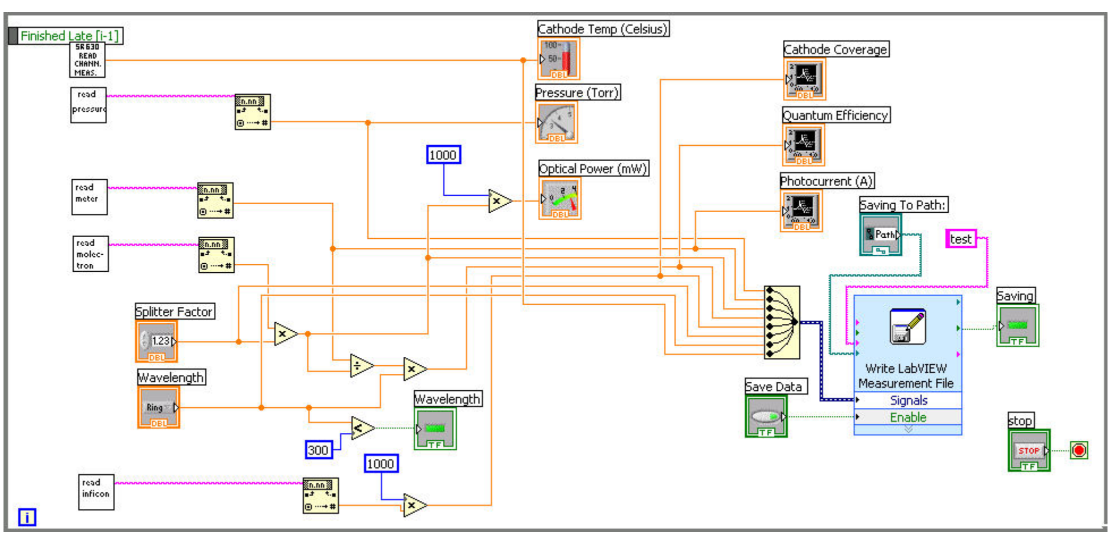

Figure 13: Labview measurement program

2.2.1 Crystal Balance

In order to determine the effect of cesium surface layers on the quantum efficiency of metal cathodes, the amount of cesium introduced must be accurately measured. This is accomplished by placing a deposition sensor adjacent to the cathode surface such that both the crystal and the cathode surface intercept the same flux of evaporated cesium atoms. It is assumed that both have identical adsorption properties and therefore an increase in mass on the sensor is presumed to have occurred identically on the cathode surface.

The sensor for Inficon's deposition monitor XTM/2 consists of a disk-shaped quartz crystal whose piezoelectric resonance is sensitive to added mass. A voltage applied to the faces of a piezoelectric crystal cause it to mechanically distort and the change in shape is proportional to the applied voltage. Due to the mass and geometry of the crystal, resonant motion can be established if the applied voltage matches the natural resonance frequency of the crystal. The resonant frequency is very sensitive to slight changes in mass and can be used to detect the addition of less than an atomic layer of adsorbed material. An RF source sweeps through a range of frequencies and as mass is increased, the observed resonant frequency will decrease. The Inficon crystals have a starting frequency of 6.0 MHz and register a shift of 2.27 Hz when 1 Ångstrom of aluminum is deposited. For films less than $2\mu\mathrm{m}$ thick, the frequency shift is linear and obeys Saurerbrey's equation:

$$f_c = f_q - \sigma m \tag{1.6}$$

where f_q is the fundamental resonance frequency of an unexposed crystal, f_c is the frequency of the coated crystal, *m* is the mass and σ is the sensitivity of the resonant frequency to a change in mass [23]. The sensitivity is an intrinsic property of the crystal and is given by $\sigma = f_q^{\,2} / NS\rho_q$, where N is the frequency constant of quartz, S is the film surface area, and ρ_q is the quartz crystal density. The XTM/2 head unit performs the calculations using user-defined parameters describing the film. Its final output is film thickness (in units of Ångstroms), found using the expression:

$$T_f = \frac{N\rho_q(f_c - f_q)}{f_q^{\,2}\rho_f} \tag{1.7}$$

where T_f and ρ_f are the film's thickness and density. Because the sensor (shown in Figure 14) is very sensitive to changes in temperature, a water circulation system was installed to minimize temperature fluctuations. When excessively thick films are deposited (on the order of microns) the crystal's resonant motion becomes unstable and varies between neighboring modes of different frequencies. This is a sign that the crystal sensor has reached the end of its usable life and must be replaced (this was necessary only once in this experiment). A photo of the mounted crystal sensor is shown in Figure 15. Note that the cathode assembly sits directly beneath the sensor so that both are the same distance from the evaporation source.

Figure 14: Quartz crystal sensor unit

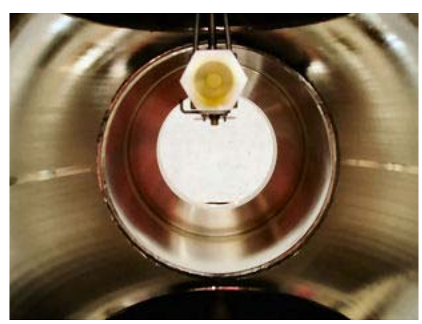

Figure 15: Mounted Deposition Sensor

2.2.2 Residual Gas Analyzer

While an ideal vacuum system for photoemission experiments should have as low a background pressure as possible, the *composition* of the residual gas in the system is just as critical. Water and carbon monoxide, for example, are highly detrimental to the lifetime and performance of cesiated cathodes. A residual gas analyzer (RGA) was installed on the system to measure not only the total background pressure, but also the gas composition at various stages of the experiment.

An RGA is essentially a mass spectrometer that ionizes gas molecules and separates the resulting positive ions according to mass, while measuring the ionic current corresponding to each mass. This ionic current is a representation of partial pressure. The mechanism responsible for separating ions according to their mass is the quadrupole mass-filter, consisting of four long rods, operated by a combination of RF and DC voltages. The RF field's magnitude and frequency determine the mass/charge ratio of ions permitted to pass through without striking the rods, while the RF/DC voltage ratio determines filter selectivity. Ions that pass through the filter constitute a current measured by a sensitive electrometer.

2.2.3 Pressure Measurement and Management

In addition to the RGA, the system is equipped with a Bayard-Alpert ion gauge and a thermocouple gauge to enable measurement over the entire range of pressures from UHV to atmosphere. A Labview program monitors pressure via a Granville-Phillips 307 controller during bakeout, outgassing, or measurement processes and interrupts the process if the pressure exceeds a threshold of 1×10^{-7} Torr. The gauges are calibrated for nitrogen readings, so when other gases were intentionally introduced during ion bombardment cleaning, it was important to use a scaling factor to obtain true pressure.

2.2.4 Photoemission Measurements

A critical measurement in this experiment is quantum efficiency, the ratio of photoemitted electrons to incident photons. Measurement of small currents on the order of hundreds of nanoamperes is accomplished using an HP-0000 in the configuration shown in Figure 16. The anode is kept at a potential of +286V relative to the cathode via a battery bank in series with a current limiting resistor and the HP meter. Both anode and cathode are electrically isolated from the chamber, which is kept at ground potential.

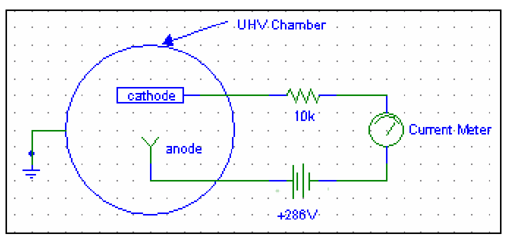

Figure 16: Photoemission measurement circuit

Because cesium atoms are deposited throughout the chamber, not just the cathode surface, care must be taken to ensure that the laser is focused only on the cathode to prevent photoemission from other metallic components within the chamber. As the CW laser strikes the cathode, electrons are emitted and accelerate toward the anode where they constitute a photocurrent that is detected by the meter. This measurement must occur during cesium evaporation, so care must be taken to ensure that only neutral cesium ions arrive at the cathode surface. This is accomplished by placing a screen at -90V relative to ground in front of the sources (which also sit at ground potential) to draw off any ions that emerge along with neutral cesium atoms.

2.2.5 Temperature Measurements

Cathode temperature is measured using a type K thermocouple mounted in the heater assembly and is connected to an SRS SR630 thermocouple monitor which is accessible via GPIB. Thermocouples attached to the chamber for monitoring the bakeout process are also connected to this instrument.

2.3 Optics

Two CW lasers with wavelengths 405nm and 531nm are used in this experiment to make quantum efficiency measurements. The lasers, together with a thermopile sensor and splitting mirror, are mounted on an optical breadboard with precision stages to permit adjustment of its position in both the vertical and horizontal directions.

2.3.1 Optical Power Measurement

In order to determine quantum efficiency, both photocurrent and optical power are required. A Molectron EPM1000 light meter using the PM3Q thermopile sensor is used to determine the power of the lasers. Quartz viewports are used in this experiment to prevent attenuation of the blue laser and it is important to consider the reflectivity of viewport surfaces since the power relevant to quantum efficiency is that arriving at the cathode surface. Approximately 3.5% of light incident on each surface of the quartz window is reflected, so only 93% of the beam arriving at the viewport is transmitted to the cathode. In the case of the green laser, a 15% beam splitter is used to monitor power in real time, so only 79.2% of the original power arrives at the cathode surface. Labview takes these values into account when calculating quantum efficiency for both lasers (the user selects which wavelength will be used in a particular experiment). Figure 17 shows the green Nd:Yag laser mounted on the optical bench with the beam splitter and Figure 18 shows the blue diode laser aimed directly at the viewport.

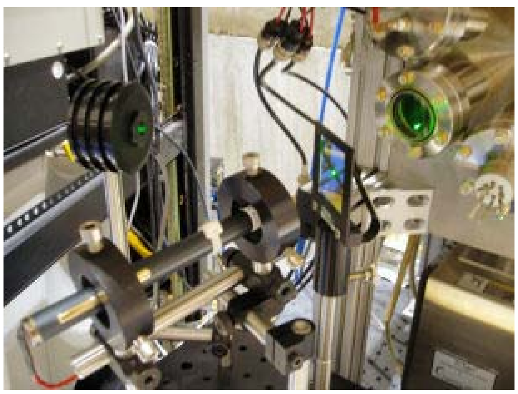

Figure 17: Green Nd:YAG laser setup

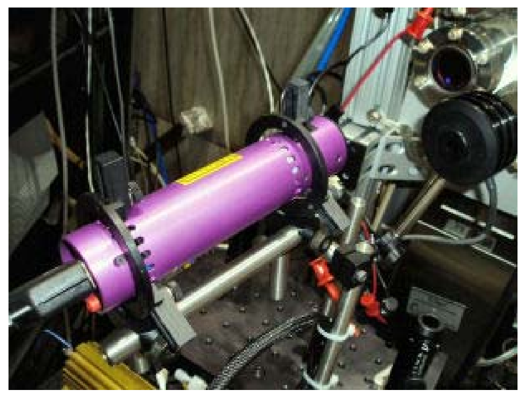

Figure 18: Blue diode laser setup

2.3.2 Frequency Doubled Nd:YAG Laser

The first laser used in this experiment is an inexpensive diode pumped Nd:YAG operating at < 5mW at 532nm. In this type of laser, neodymium ions are situated in an yttrium aluminum garnet (YAG) crystal $Y_3Al_5O_{12}$ which is optically pumped at 1064nm with a diode laser. The resulting radiation is then frequency doubled to 532nm using a potassium titanium oxide phosphate (KTP) $KTiOPO_4$ crystal. All this is housed in the small enclosure the size of a laser pointer. The emitted beam is <2.5mm in diameter, with a beam divergence <1.5mrad. While this laser is inexpensive, it is not stable in terms of output power. Figure 19 shows the power fluctuations in the green laser over a period of 1000 seconds. Because the laser power changes with time, a beam splitter was installed to direct a portion of the beam to a detector to permit real-time measurement. The detected power, together with the photocurrent at that particular instant, is used to calculate quantum efficiency. Figure 19 shows that over long periods of time, the optical power of the green laser decreases dramatically from nearly 10mW to less than 3mW. This wide variation makes QE measurements difficult, so a blue laser was introduced in order to simplify measurements and to increase the photocurrent signal (due to shorter wavelength).

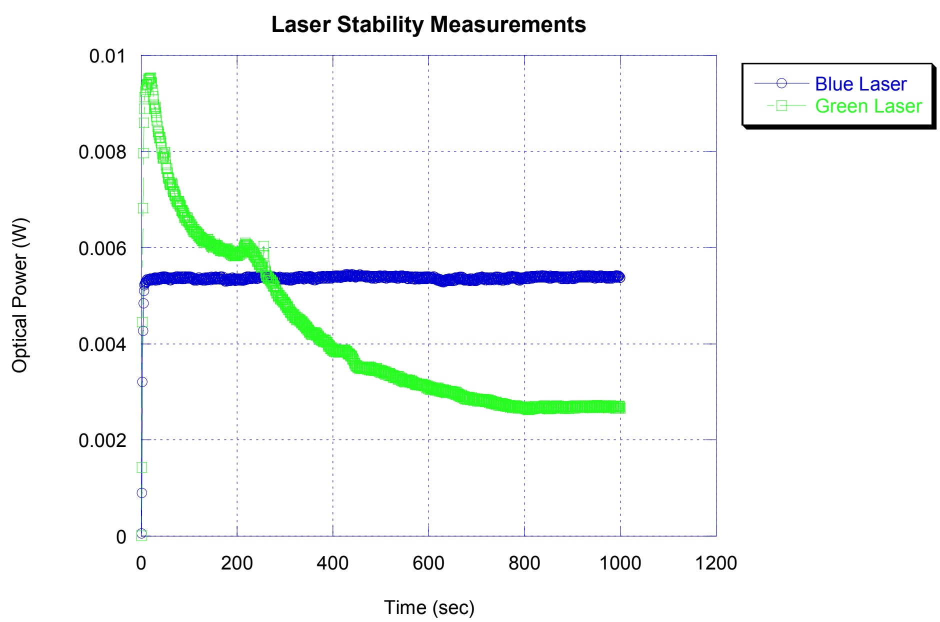

Figure 19: Laser power vs. time for green and blue

2.3.3 Blue Diode Laser

The blue laser operates at a constant power level of 5.0mW and wavelength of 450nm. Because the beam is produced by an edge-emitting diode, the beam is elliptically shaped $(4.4\text{mm}\times 1.4\text{mm})$ and the beam divergence is 0.4×0.6 mrad. The advantage with this laser (as shown in Figure 19) is that the power fluctuation is less than 1%. It is thermo-electrically cooled using microprocessor-driven Peltier junctions, a heat-sink, and a fan. A trigger signal can be sent to the laser to key the diode on and off, yet the microprocessor and cooling module remain active to maintain constant temperature. The Labview measurement program uses this feature to toggle the laser on and off at specified intervals to check that the current measured by the meter is entirely photocurrent. Figure 20 shows the performance of the laser with respect to this keying. Note that with each cycle, the laser attains the same maximum output power.

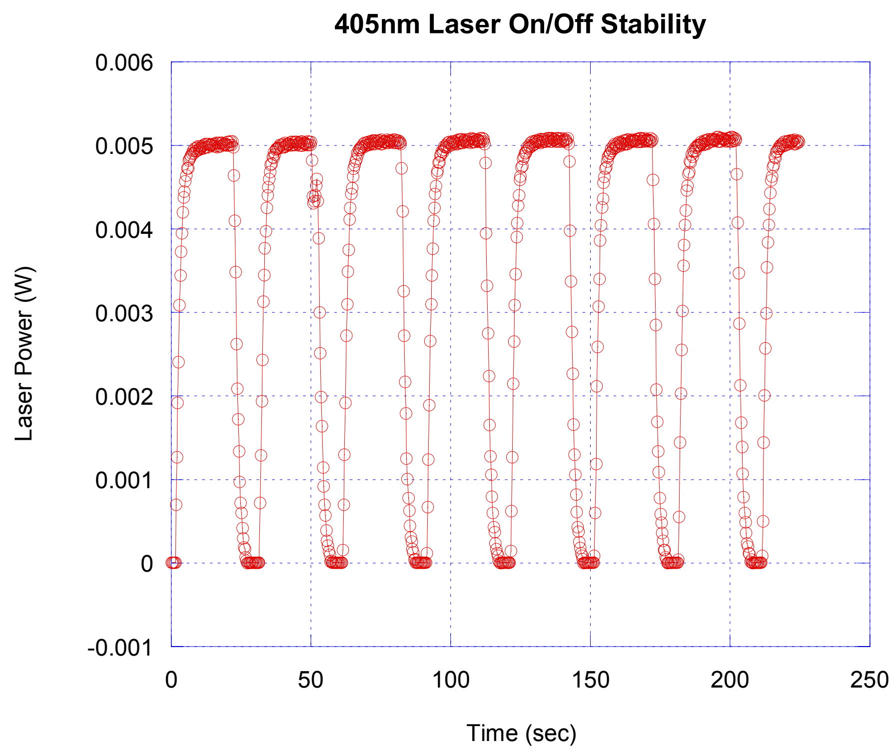

Figure 20: On/off keying of blue laser diode

In the case of both lasers, the beam was expanded to a diameter of about 5mm to assure that localized heating of the cathode surface would not be a factor in the photoemission process.

2.4 Cathode Preparation

2.4.1 Heat Treatment

The cathode heater consists of a nichrome filament alumina-potted inside a molybdenum chassis capable of reaching temperatures in excess of $1200^{\circ}C$. The process of heating the cathode to high temperature is called "firing" and is the preliminary surface treatment in preparation for evaporation of surface films. Tungsten was fired at $1200^{\circ}C$ for 8 hours prior to evaporation, while silver (due to its lower melting temperature of $930^{\circ}C$) was fired for the same length of time at $650^{\circ}C$.

Because the cathode assembly is connected to the chamber only through thin ceramic standoffs and electrical feedthroughs, it is thermally isolated and takes hours to cool down, as shown in Figure 21.

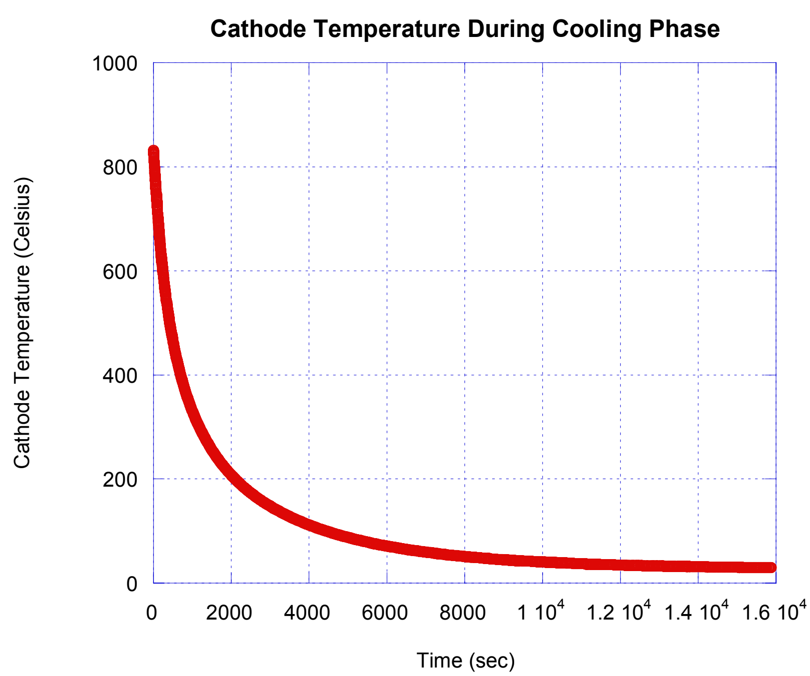

Figure 21: Cathode temperature after heat treatment

2.4.2 Argon Discharge Cleaning

Following examples in the literature glow discharge treatments were performed in an attempt to remove contaminants, such as hydrocarbons, from the cathode surface [24],[25],[26]. Glow discharge cleaning (GDC) involves formation of low energy plasma, causing energetic ions to sputter adsorbed molecules or atoms from the surface to be cleaned. The plasma formation occurs under specific gas pressures and ion currents and can be achieved using either RF or DC fields. For convenience, DC excitation was chosen in this experiment. De-excitation of the gas molecules produces visible light emission (usually purple in color) at the electrode with lower potential. In this experiment, a potential of +300V is applied to the chamber relative to the cathode surface. Over a specific range of pressures, plasma occurs and the positively charged argon ions are accelerated toward the lower potential surface. The resulting collision process (ion bombardment) cleans the surface and produces the familiar glow of GDC.

The glow discharge is maintained by secondary electron emission, so GDC cannot persist over an arbitrary range of pressures, but rather those which can sustain a critical current density of about $1\mu\text{A/cm}^2$ [27]. When the current density exceeds $100\mu\text{A/cm}^2$ arcing may occur, causing unwanted deposition of metal. To prevent arcing, a $2\text{k}\Omega$ current limiting resistor was placed in series with the source and electrodes.

The first GDC attempts involved a static discharge, meaning that no pumping was performed during the cleaning process, in order to determine the range of pressures and voltages over which the discharge is sustained. A roughing pump with a conductance limiting valve was later used to slowly pump the argon atmosphere while fresh argon was bled into the system at the same rate using a needle value. Table 4 shows the argon GDC parameters used in this experiment.

Voltage	350VDC
Current	30mA
Pressure	3×10^{-2} Torr
Chamber Temp	180°C
Cathode Temp	$< 600^{\circ}$C
Gas Flow	0.2 cc/s

Table 4: Argon gas discharge cleaning parameters

Because the electrode at the lower potential will experience discharge cleaning, it is simple to interchange the potentials applied so that various surfaces throughout the vacuum chamber are selectively cleaned. If the cathode assembly was held at +350V relative to the vacuum chamber, then the plasma was sustained uniformly throughout the chamber, cleaning the walls and all other surfaces at the lower potential. In this manner, the background pressure was further reduced by removing adsorbed molecules within the chamber prior to a bakeout.

2.4.3 Hydrogen Discharge Cleaning

While argon discharge cleaning and firing of the tungsten substrate effectively removes organics, carbon monoxide, and carbon dioxide, the oxide layers that form during exposure to air are not as easily removed. This is because argon cleaning involves a kinetic process whereby adsorbed molecules are dislodged from the surface via collision events. This type of cleaning is effective only when contaminants are loosely bound to the surface. Hydrogen discharge cleaning, however, is used to clean surfaces using a *chemical* process. The advantage is that hydrogen ions chemically react with contaminates and surface oxide layers to form various volatile compounds which are then pumped out of the chamber. Figure 22 shows the valves and steel tubing used to introduce high purity hydrogen gas into the test chamber (steel tubing and hardware was used to reduce contamination).

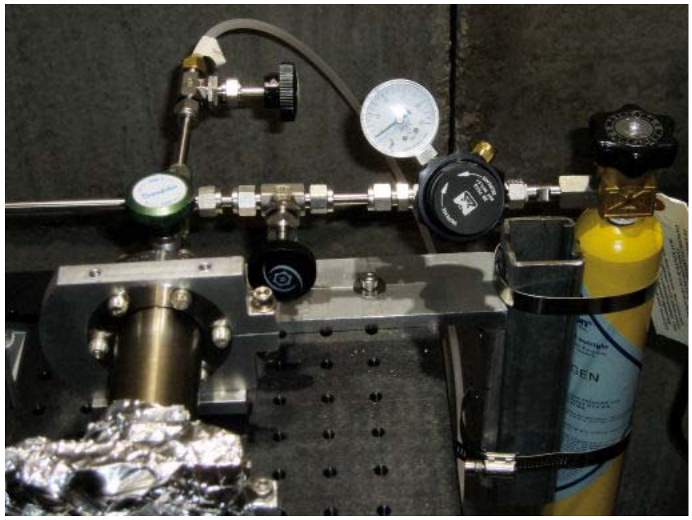

Figure 22: Hydrogen gas apparatus

2.4.4 Evaporation Techniques

After the cathode surface is prepared through heating and glow discharge cleaning, cesium evaporation on the surface can begin. The cesium sources shown in Figure 5 are activated with a current of 6.0A when new and 7-8A after about 10 temperature cycles. For new sources, the temperature must be gradually increased prior to activation to outgas the source. A programmable DC power supply is used via Labview to slowly increment the current passing through the source. Labview prompts the user for a target pressure and then adjusts the rate of increase in source temperature to stay within that pressure limit. If pressure exceeds the given threshold, the temperature is decreased until pressure is sufficiently reduced and the outgassing process continues. The program will shut down the outgas procedure if the deposition monitor registers 2 Ångstroms of cesium during this stage, signaling that the source has activated and is ready to use. Figure 23 shows the outcome of the outgas process.

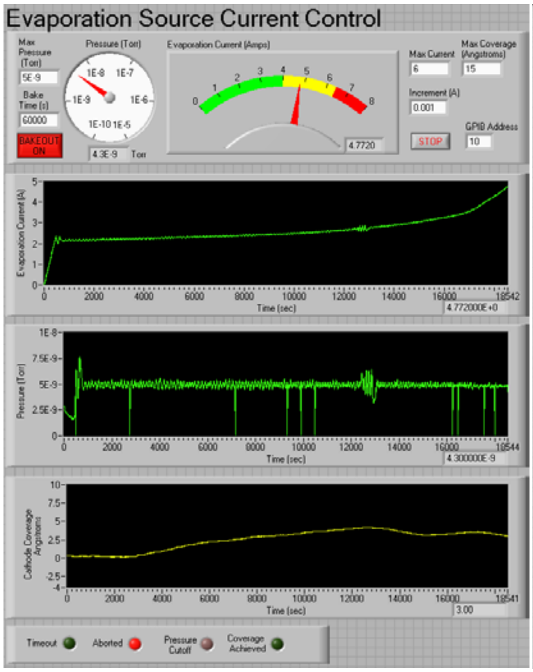

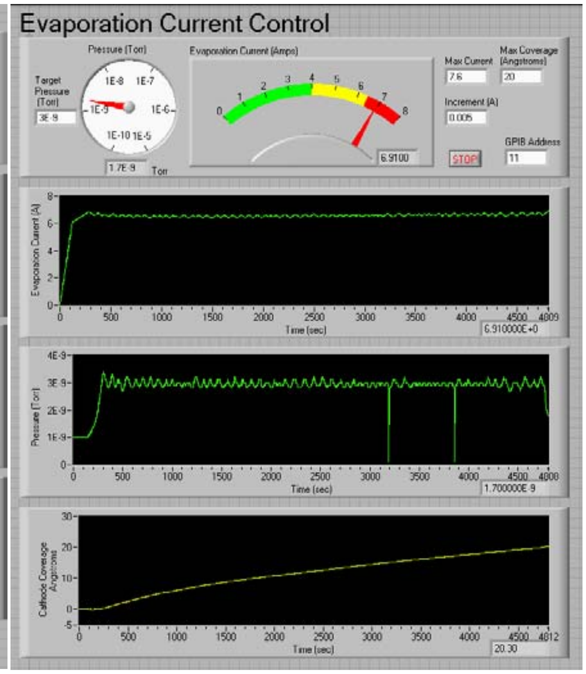

Figure 23: Cesium outgas process **Figure 24: Cesium evaporation process**

Notice that the pressure was kept at about 5×10^{-9} Torr during outgassing of the source and 3×10^{-9} Torr during cesium evaporation. Figure 24 illustrates the process of evaporating a 20 Ångstrom thickness of cesium and shows that 6.5A was required to achieve this coverage. Note that the coverage vs. time plot for evaporation is not linear, meaning that the source is slowly running out of cesium and is nearing the end of its usable life. The lifetime of the cesium sources varied from between 10 to 15 temperature cycles, and it was observed that each consecutive cycle required a higher activation current than the previous. Un-used cesium sources were kept in a desiccator to prevent moisture contamination from being introduced into the system.

Chapter 3: Experimental Results

Although the emphasis of this section is on the experimental results of cathode fabrication, the performance of the test chamber itself will be briefly discussed because of its role in future research of dispenser cathodes.

3.1 Test Chamber Performance

During the setup of the chamber, many new vacuum components were added and repositioned. A helium leak-check was performed, however, and no detectable leaks ($<1\times10^{-10}$ Torr) were found. Furthermore, the bakeout procedures and discharge cleaning were effective in removing adsorbed gas molecules.

3.1.1 Bakeout Results

Figure 25 shows the background gas composition prior to bakeout, but after 24 hours of rough pumping. Note the large amounts of water, and CO.

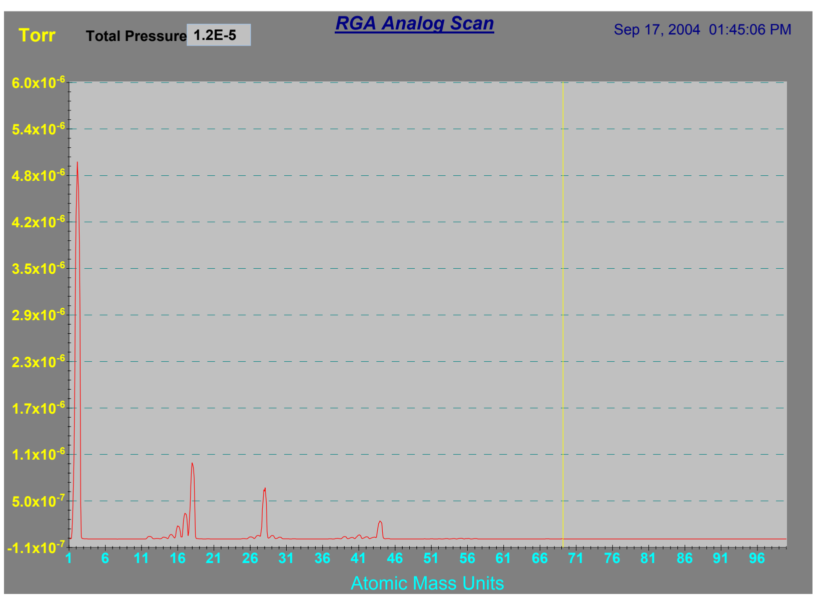

Figure 25: Background composition prior to bakeout

Figure 26 shows the background gas composition of the chamber after about 16 hours of bakeout during rough pumping only (total pressure of 1.1×10^{-6} Torr).

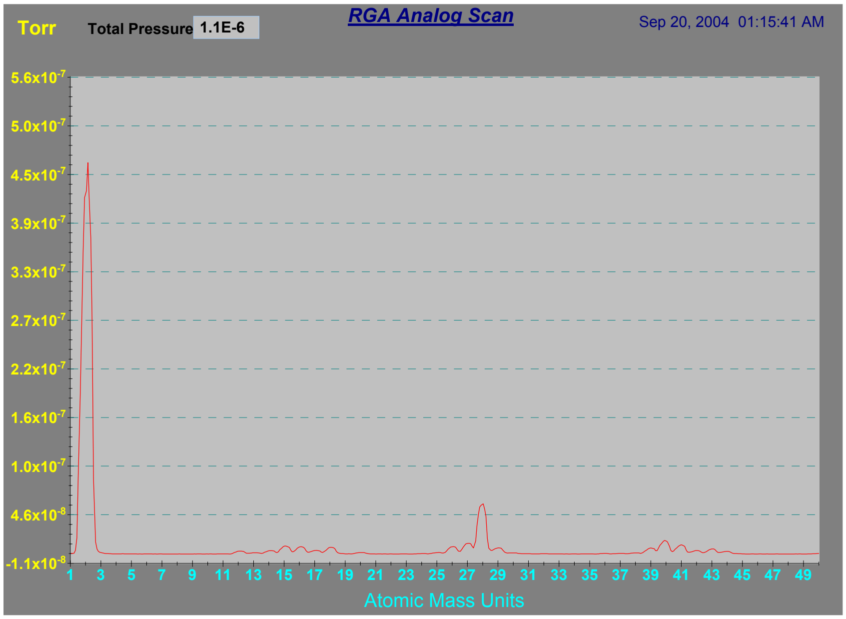

Figure 26: Background composition after bakeout during rough pumping

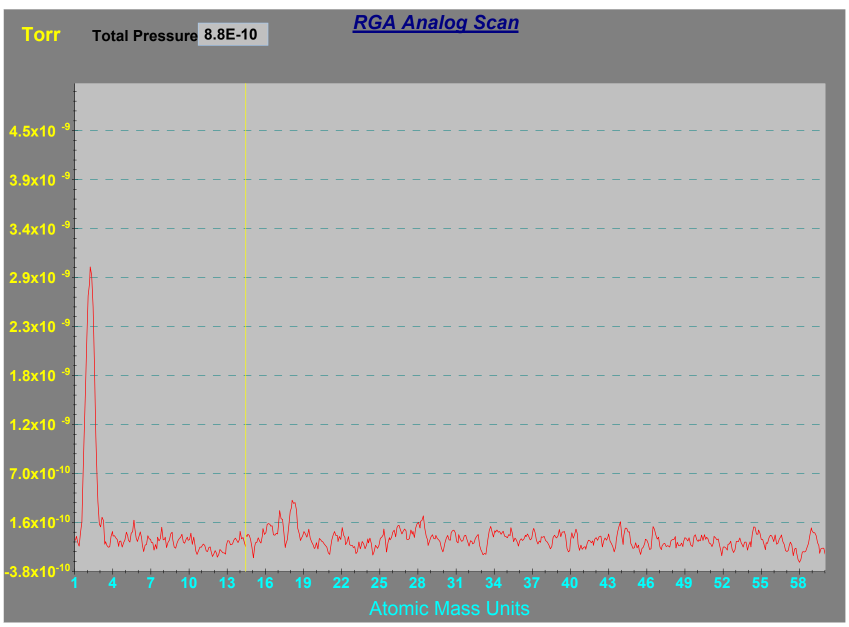

Figure 27: Background composition after bakeout during ion pumping

The majority of the background gas before and after ion pumping is hydrogen, which has no effect on the photoemission measurements. Hydrogen is absorbed by stainless steel and is slowly released into vacuum. Figure 26 shows that baking the system during rough pumping reduces the amount of water and CO by two orders of magnitude. Continuing the bake process during ion pumping results in a very clean system having a background pressure of 8.8×10^{-10} Torr, as shown in Figure 27. Again, notice that the contaminants detrimental to photoemission, such as water and CO, show partial pressures less than 2×10^{-10} Torr.

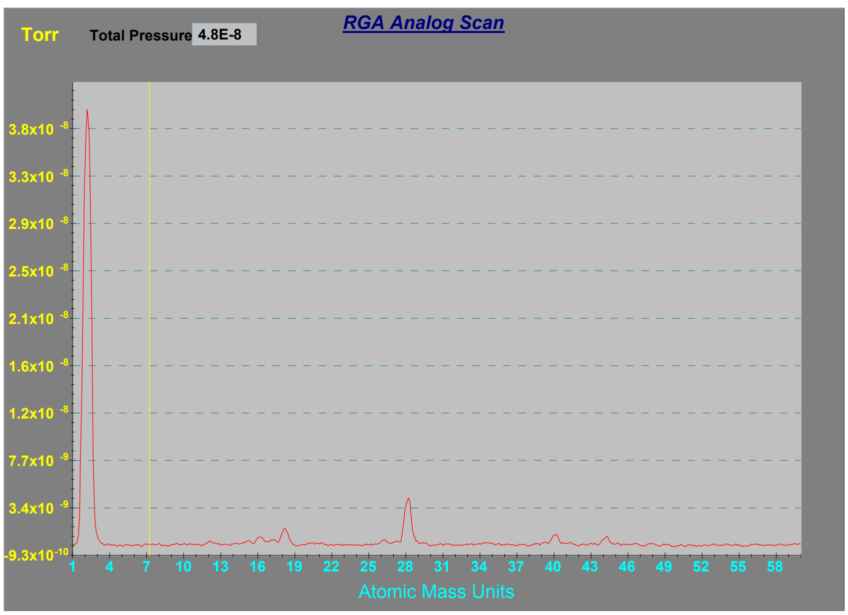

Figure 28: Background composition after cesium source outgassing

Figure 28 shows the background composition during outgassing of a new cesium source. It is apparent that CO, H_2O, N_2O, and Ar are the dominant contaminants present in the cesium sources.

3.1.2 Discharge Cleaning Results

In measuring photocurrent and quantum efficiency (discussed later) it was seen that the process of argon cleaning did not improve photoemission from cesiated tungsten, as there was no change in QE. Argon cleaning did, however, lead to a reduced background gas pressure of $< 3\times10^{-10}$ Torr (found by averaging the pressure readings from the ion gauge, RGA, and ion pumps). This is lower than the pressure achieved using bakeouts alone. So while argon cleaning did not significantly affect the surface of the cathode, it was adopted as a regular step in the chamber pumpdown process after new equipment was added. Again, because argon atoms are large and electrically neutral, the ion pumping after an argon flush was particularly slow and required more than twice the amount of pumping time as a nitrogen flush.

Hydrogen appeared to significantly affect the tungsten surface, as the quantum efficiency nearly doubled after a hydrogen treatment process. Further investigation is required to confirm this completely, however, due to problems encountered in using hydrogen in the chamber. Specifically, the sensor in the crystal balance fails when in a hydrogen atmosphere for extended periods of time. After a system teardown, the sensor was disassembled to determine the cause of failure. It was apparent that the leaf springs holding the quartz crystal in place had lost their tension and were not making electrical contact with the gold film on the sensor. After repairing the sensor and returning the system to a hydrogen atmosphere, the same failure occurred (repeatedly). Although a new sensor is on order, it appears that the hydrogen has a weakening effect on the metal used to fabricate the sensor's springs. When this detail is worked out, the effect of hydrogen discharge cleaning can be determined more accurately.

3.2 Quantum Efficiency Measurements

In this experiment, quantum efficiency is found by illuminating the cathode with light of a given intensity and the resulting photocurrent is measured by a sensitive current meter. Because the observables are current and power, it is necessary to relate these to quantum efficiency, defined as the ratio of the number of photoemitted electrons, N_e, to incident photons, N_p:

$$QE = \frac{N_e}{N_p} \tag{1.8}$$

The ratio of photocurrent to optical power is given by:

$$\frac{Current}{Power} = \frac{q/s}{E/s} \tag{1.9}$$

Dimensional analysis shows that by multiplying this ratio by the energy per photon and dividing by the charge of an electron the ratio of photoemitted electrons to incoming photons is:

$$\frac{N_e}{N_p} = \frac{q/s}{E/s} \cdot \frac{hc}{\lambda} \cdot \frac{1}{e} \tag{1.10}$$

Therefore, given photocurrent *I* and optical power *P*, the quantum efficiency is:

$$QE = \frac{I}{P} \cdot \frac{hc}{\lambda e} \tag{1.11}$$

If measurements are made in SI units, the factor above is $\frac{hc}{\lambda e} = 2.325 \text{ J/C}$ for green light (532nm) and 3.053 J/C for blue (405nm). Having expressed quantum efficiency in terms of experimental quantities, the photocurrent vs. coverage data obtained from Labview can be converted to QE vs. coverage data.

3.2.1 QE vs. Coverage Results

In this section, the term 'coverage' refers to the amount of cesium evaporated on the tungsten surface and is provided by the Inficon XTM/2 in terms of thickness in Ångstroms. The most striking result of this data is that as cesium is evaporated onto the cathode surface, the quantum efficiency steadily increased and reaches a peak before declining and leveling off. This behavior was confirmed in five separate trials involving both the green and blue lasers. Because the green laser produces such small photocurrents, the digital noise of the meter made this peak difficult to discern, but the blue laser made this peak very clear. Figure 29 shows raw measurements of QE (%) versus thicknesses at 405nm.

Because the deposition monitor has can resolve only to a tenth of an Ångstrom, it rounds all intermediate thickness values such that, for example, 1.12 Ångstroms is reported as 1.1. Thus, in Figure 29 there are a number of different QE values corresponding to each thickness value (each of which are separated by a distance 0.1 Ångstroms). A peak in QE is still discernable, however, and occurs when about 3 Ångstroms of cesium have been deposited. The peak is clearer if QE values corresponding to a unique thickness are averaged together. This representation is shown in Figure 30. The error bars are chosen by observing the behavior of QE when no cesium has been deposited. At vanishingly small currents, the meter reported negative values (and therefore a negative QE) due mostly to digital noise. Because QE cannot be negative, the error in the measurement is assumed to be the extent to which QE was reported negative when no photoemission was present, about $\pm 0.0035\,\%$.

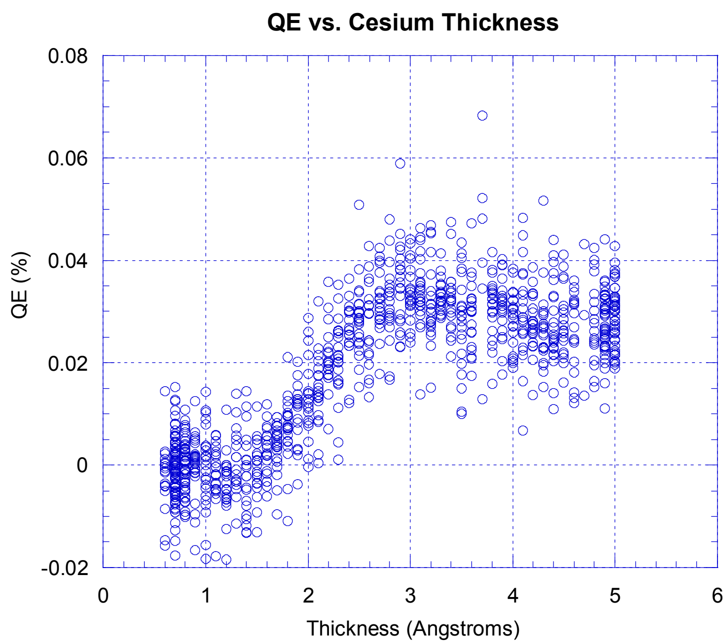

Figure 29: QE vs. Cesium Thickness

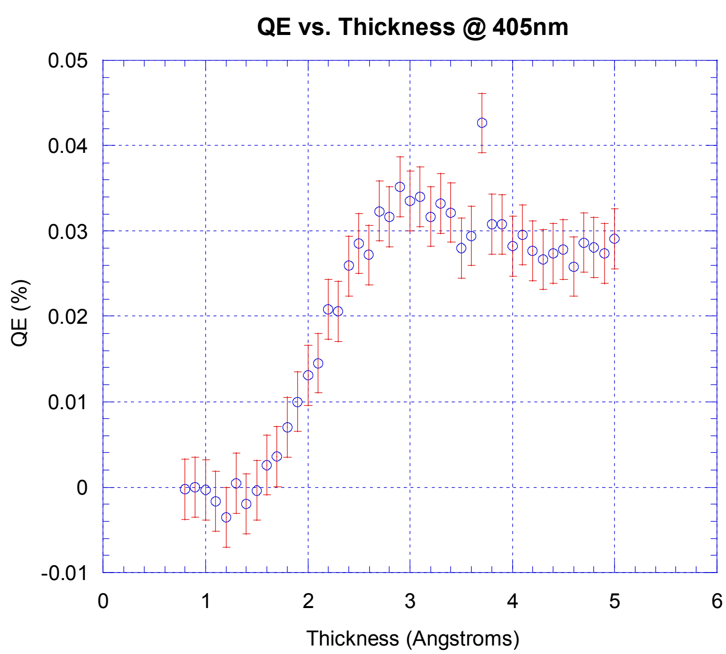

Figure 30: QE vs. Cesium Thickness (averaging applied)

3.2.2 QE vs. Temperature

Because photoemission depends strongly on the amount of cesium at the cathode surface, any process that alters this parameter will in turn alter the quantum efficiency. Raising the cathode temperature will accelerate desorption of cesium from the cathode surface, resulting eventually in complete removal of the cesium layer. In this experiment, the cathode was heated according Figure 31.

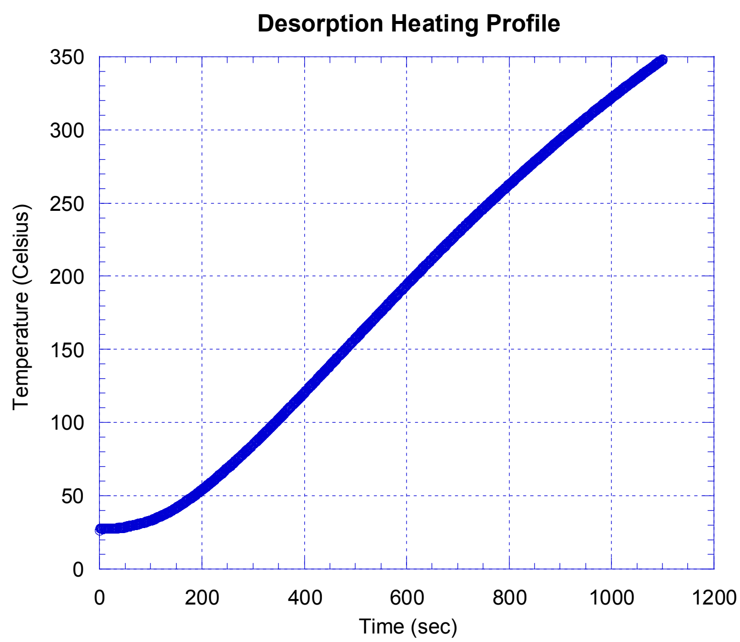

Figure 31: Cesium desorption heating profile

Using this heating process, various thicknesses of cesium ranging from 3 to 20 Ångstroms were slowly removed from the surface and the effect this had on quantum efficiency was observed. As shown in the following graphs, as the cesium was removed, the QE passes through a maximum that apparently corresponds to thicknesses which optimize photo-yield (in agreement with Figure 29).

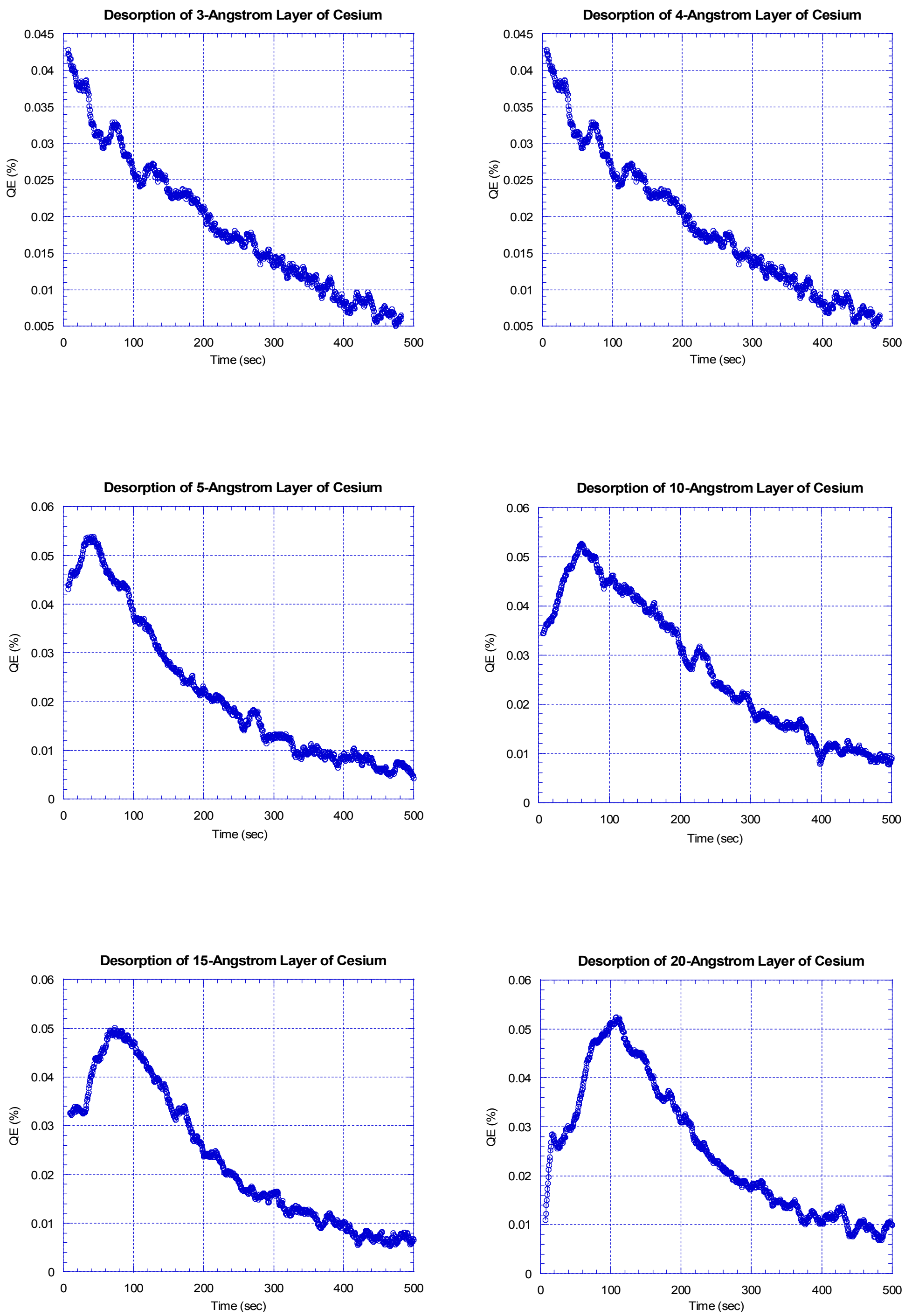

Figure 32: QE vs. time - desorption of various cesium layer thicknesses

Figure 32 shows the effect of heating on QE of heating films ranging in thickness from 3 to 20 Ångstroms. Each film was subjected to an identical heating process for 500 seconds. It is apparent from the first and second graphs that the optimal thickness for QE is less than or equal to about 3-4 Ångstroms, because as cesium films of this thickness are removed via the heating process, the QE decreases monotonically without passing through a maxima. The graphs corresponding to increasing thicknesses of the cesium layer (5, 10, 15, and 20 Ångstroms, respectively) all exhibit QE maxima, and at increasingly longer heating times. This is presumably because thicker layers of cesium require longer amounts of time to desorb and cross through the optimal thickness where QE is maximized.

3.2.3 Effect of Adsorbed Oxygen on QE

Various experiments [28],[29] have shown that pre-adsorbed layers of oxygen (i.e. layers that form prior to cesiation) further reduce the workfunction of cesiated tungsten to less than 1eV. In an attempt to study this effect, known amounts of ultra-pure oxygen were introduced into the chamber after heat treatment of tungsten, but prior to cesium evaporation. No appreciable difference in quantum efficiency was noticed, however, for any of the amounts of pre-adsorbed oxygen. It may be that an oxide layer is already on the tungsten and is masking the effect of slight additions of pre-adsorbed oxygen.

3.2.3 Effect of Surface Treatment on QE

In all measurements involving quantum efficiency, the tungsten substrate was heat treated for 8 hours at $1200^{\circ}C$ prior to cesium deposition. If this procedure was not performed (i.e. cesium evaporated directly onto tungsten that was exposed to atmosphere) no photocurrent whatsoever was observed for any thickness of the cesium layer.

3.3 Lifetime Measurements

Improving the quantum efficiency of photocathodes is hardly worthwhile unless it can be maintained for a practically useful lifetime. This project, in preparation for future dispenser cathode development, assumes that a periodic rejuvenation period is an acceptable compromise to extensively long lifetimes. Figure 33 shows a typical cathode lifetime observed in a vacuum of $<1\times10^{-9}$ Torr using 405nm light. In this experiment, 10 Ångstroms of cesium were evaporated onto a cleaned tungsten surface and the QE was measured at room temperature over time.

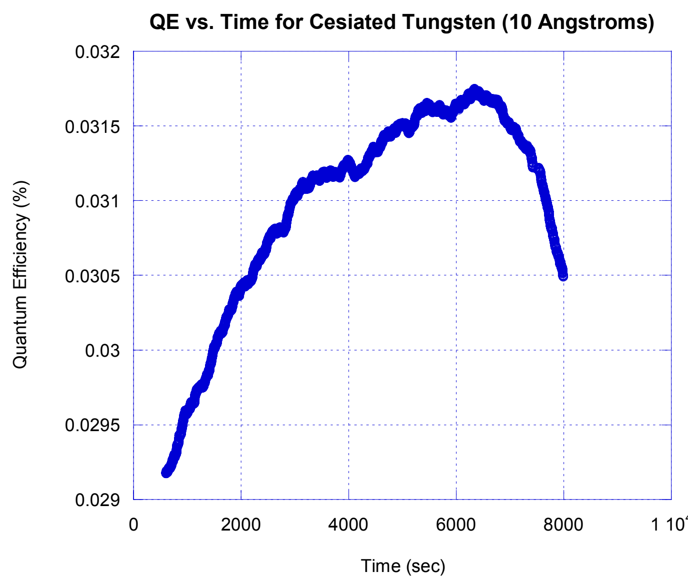

Figure 33: Lifetime of cesiated (10 Ångstroms) tungsten cathode

As with the previous graphs, a peak is observed that corresponds to a thickness where photoemission is optimized. Desorption occurs even at room temperature, so one mechanism that acts to reduce QE with time is the simple fact that cesium is slowly leaving the surface. The dominant effect shown in Figure 32 is simply that which is intentionally achieved through heating. Another factor limiting cathode lifetime is ion back-bombardment. It was observed that if the entire chamber was used as an anode (instead of the annular disk shown in Figure 11), the cathode lifetime is extended by about 20%. This is presumably due to the fact that contaminants are generated near the anode as electrons from the cathode impinge on the surface. The close proximity of the anode to the cathode allows some of these impurities to contaminate the photosensitive surface layer and reduce lifetime. Using the chamber as an anode separates the cathode from impurity generation sites, effectively lengthening the lifetime of the cathode.

Chapter 4: Analysis

4.1 Workfunction

It was observed in section 3 that a layer of cesium deposited on a clean tungsten surface allows photoemission to occur at visible wavelengths. Photon energies in the visible correspond to about 2-3eV, about half that required to induce photoemission from tungsten alone ($\phi_W = 4.65\text{eV}$). Thus, photoemission from tungsten is impossible using anything close to visible light.

4.1.1 Workfunction Reduction

The workfunction for cesiated tungsten (at least when only monolayer thicknesses of cesium are present) is about 1.5eV, which is sufficiently low to allow photoemission from green light. Thus, an adsorbed surface layer of cesium onto a tungsten substrate causes the overall workfunction of the system to fall below that of either cesium or tungsten alone. While the exact shape of the spectral response of various cesiated metals will vary, the same basic property is the same: the cesium layer dramatically lowers the workfunction. A primary goal in designing a photoinjector is to produce a required electron beam current with minimal cost and complexity. For prompt emission, beam current is directly proportional to drive laser power:

$$I(A) = \frac{\lambda(\mu m)}{124} \cdot P_{laser}(W) \cdot QE(\%) \qquad (1.12)$$

Of utmost importance in a practical photoinjector is the availability and required complexity of the drive laser. Very high power, mode-locked UV lasers are not available, so for cathodes with high workfunctions, beam current is limited by the low power of the drive laser. By reducing the workfunction of the cathode, however, lasers with higher power but lower photon energy can be used. Table 5 shows the photon energies of various commonly used lasers.

λ(nm)	Description	hf (eV)
1064	Nd:YAG fundamental	1.17
920	Ti:Sapphire fundamental	1.34
532	2^{nd} Harmonic Nd:YAG	2.33
405	Blue diode laser	3.06
355	3^{rd} Harmonic Nd:YAG	3.49
266	4^{th} Harmonic Nd:YAG	4.66

Table 5: Photon energies of common wavelengths

For most accelerator applications, the Nd:YAG harmonics are most common, which is why the power is so limited at higher wavelengths. These wavelengths are obtained using a nonlinear conversion process that varies with $(\text{laser intensity})^n$, where n is the harmonic number [30]. So fluctuations in the laser intensity become more of a problem at higher harmonics. Any unwanted fluctuations in the drive laser intensity are identically replicated in the electron beam. This is obviously detrimental, because beam quality was the very parameter photoemission was intended to improve.

The conversion crystals are only 35% efficient on average and the waste energy, which manifests as heat, can further perturb the conversion process [30]. Two crystals are required to convert IR into UV, and because the process is so inefficient ($\eta = 10\%$), high laser power in the UV is not possible. For these reasons, the second harmonic (532nm) is generally regarded as an optimal wavelength, and strong emphasis is instead placed on improving QE at this photon energy.

4.1.2 Surface Dipole Moments

The mechanism responsible for lowering the workfunction is the introduction of a strong electric field at the atomic surface interface. Because cesium is highly electropositive, it easily yields its outer valence electron to the tungsten bulk when adsorbed on the surface. The resulting positive charge residing just outside the tungsten surface induces an image charge situated the same distance inside the surface. This produces a dipole moment normal to the surface and establishes a strong electric field near the vacuum interface. Electrons are effectively assisted by this field in crossing the potential barrier, such that the energy they need to cross over (i.e. workfunction) is reduced.

Figure 34 depicts the process of evaporating cesium atoms onto a tungsten substrate to create the dipole moments. Less than a monolayer of cesium coverage is depicted for reasons explained in the next session. It is possible to evaporate more than a monolayer of cesium, but doing so does not increase the dipole effect that assists electrons in their departure from tungsten.

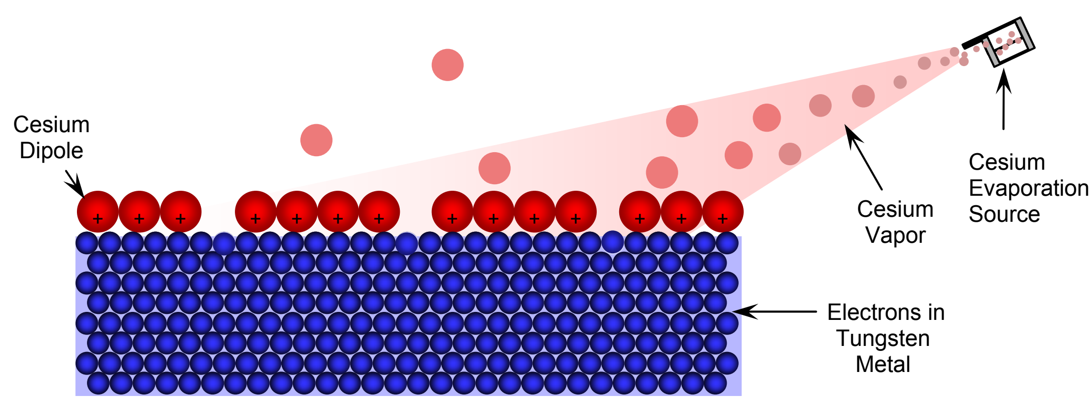

Figure 34: Surface dipole moments from adsorbed cesium

4.1.3 Pre-adsorbed Oxygen Layers

It has been demonstrated that an additional lowering of the workfunction can be achieved by placing a layer of oxygen in-between the substrate and the photosensitive layer [28]. Recall that the electric field $\vec{E}$ of an electric dipole is directly proportional to the charge separation distance $\vec{d}$:

$$\vec{E} = \frac{q\vec{d}}{4\pi\varepsilon_0 r^3} \tag{1.13}$$

Thus, increasing the separation between the positive cesium ion and its image charge within the bulk substrate will augment the electric field seen by an electron near the surface. The field is oriented such that it favors the escape of the electron and into vacuum. Qualitatively, a pre-adsorbed oxygen layer simply increases the charge separation distance, which increases the dipole moment and reduces the workfunction.

The oxygen layer is formed by introducing oxygen gas into the UHV chamber for some set amount of time. The time required to form a desired thickness will obviously depend on the pressure, so a unit called the *Langmuir* was introduced to account for both time and pressure of oxygen exposure. One Langmuir is equal to 1×10^{-6} Torr$\cdot$sec of exposure [28]. For example, oxygen present in the system for 200 seconds at a pressure of 1×10^{-8} Torr is referred to as 2 Languirs of exposure. Using kinetic gas theory, the rate at which molecules impinge upon a surface at a given pressure can be calculated. Assuming an atomic surface density of about 10^{14} for metals, the time required to form a matching monolayer of adsorbed gas molecules on the metal surface can be calculated [15]. This time will depend on the sticking coefficient of the molecule, which for oxygen can be assumed to be unity because it is chemically adsorbed upon arriving at the surface. Table 6 shows the time required to obtain a monolayer (i.e. one Langmuir of exposure leads to one monolayer).

Gas Pressure (Torr)	Time Required to Form Monolayer (sec)
1×10^{-6}	1
1×10^{-7}	10
1×10^{-8}	100
1×10^{-9}	1000

Table 6: Time required to form a monolayer

Figure 35 shows the results in the literature of workfunction (eV) versus cesium deposition time for zero, 2, and 3 Langmuir exposures to oxygen [28]. Notice that in the case of the three Langmuir exposure, the workfunction was observed to be less than 1eV.

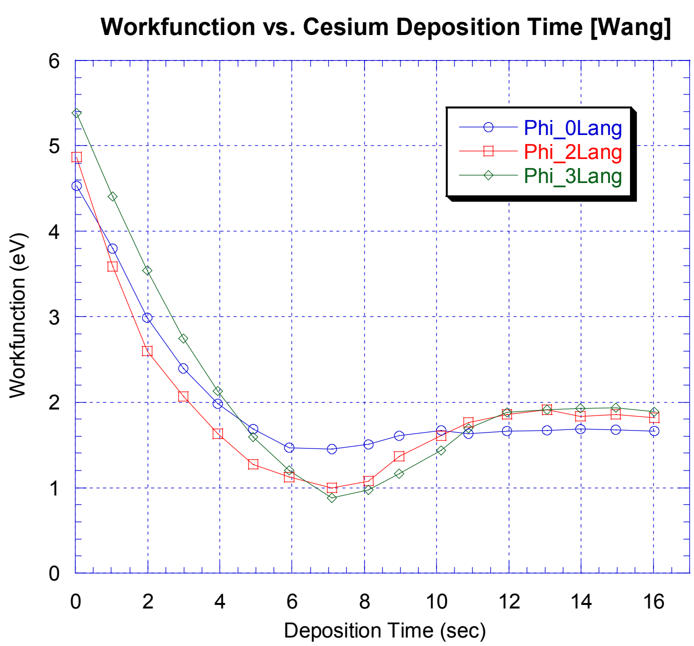

Figure 35: Workfunction reduction due to pre-adsorbed oxygen

In this project, however, exposure of tungsten to oxygen prior to cesium evaporation did not replicate this behavior. Instead, the QE (and workfunction) remained the same for zero, 2, and 3 Langmuirs of oxygen pre-exposure. A potential reason for not observing this effect is that it is very likely the tungsten surface is not atomically clean. Although the tungsten was repeatedly heat-treated up to a glowing $1200^{\circ}C$, this is not sufficient to remove surface oxides, which may mask the workfunction-reducing effects of several Langmuir exposure.

4.2 Lifetime Measurements

It is evident in Figure 33 that the lifetime of a photocathode involves several time-dynamic processes, since a maximum QE is observed (for an initial cesium deposition of 10 Ångstroms) prior to a decline in efficiency.

4.2.1 Degradation Processes

It was observed that as much as 72 hours could pass before noticeable degradation occurred in instantaneous quantum efficiency (i.e. the QE measured by turning the laser on briefly and then back off again for a long period of time). This is in contrast to the behavior shown in Figure 33, where the laser is on continuously and the QE eventually begins to decline over a period of several hours. At least two distinct processes are occurring during operation of the photocathode: 1.) evaporation of cesium from the surface, and 2.) contamination from impurities in the vacuum. The amount of impurities tends to increase when photocurrents are being generated because electrons are colliding with potentially dirty surfaces (either the anode or the chamber). Furthermore, the lower potential on the cathode will attract positively charged impurities and damage the cesium layer to some degree upon impact.

4.2.2 Evaporation Rates

The evaporation rate of cesium from the surface will change QE in several ways, depending upon how much cesium on the surface to begin with. If much more than the thickness which maximizes QE (observed in Figure 30) is initially deposited on the surface, then the surface begins to exhibit the properties of bulk cesium. Because cesium has a higher workfunction than cesiated tungsten, thick layers on the surface will increase the workfunction of the cathode and consequently reduce quantum efficiency. As this bulk-like cesium evaporates from the surface, the QE will increase as the film thickness approaches its optimum value (slightly less than a monolayer). As this critical thickness is reached, the evaporation rate changes dramatically, because the bulk evaporation rate is much faster than the monolayer evaporation rate. Furthermore, reducing the amount of cesium beneath the optimal thickness will obviously reduce QE because the surface is approaching bare tungsten once again, which has a very high workfunction and negligible QE. Thus, when the cesium surface layer is less than one monolayer, QE degrades with time but at a much slower rate.

The finite lifetime of photocathodes underscores the need for a rehabilitation process that could restore the cathode to full efficiency after degradation occurs with use. Such is the goal of the dispenser photocathode, introduced in the next chapter.

4.2.3 RF versus DC Photoinjector

The issue of lifetime and cathode contamination plays a large role in the design of photoinjectors. As mentioned in the previous section, a static potential between the chamber (i.e. anode) and the cathode accelerate positively-charged vacuum impurities into the cathode surface, causing damage. This is one of several reasons DC guns are not always the favored choice in accelerator design. In an RF gun, the field at the cathode surface varies sinusoidally at a rate impurity particles cannot follow because of their large mass, so they do not bombard the cathode as in the DC case. Conversely, RF guns have higher background pressure because of impurities leaving the cavity walls and poor pumping in resonant cavities.

Another reason DC guns may not be suitable is the large size of the accelerating section. For electrons to attain a given energy, they must be accelerated through an electric field. Because static potentials cannot become arbitrarily large without breakdown occurring, there is a minimum length an accelerating section must be to yield electrons of a given energy. Because RF guns use standing waves instead of static potentials (on actual surfaces) to accelerate electrons, the field gradients can be larger and the overall gun-length smaller.

4.3 Photoemission Theory

Before comparing experimental results with recent theory, it is helpful to appreciate the complicated relationship between the two most important quantities in this experiment: workfunction and quantum efficiency. QE is an easily measurable parameter, but depends on much more than just the workfunction of a metal. Because it is a ratio of photoemitted electrons to the number of incident photons, it must encompass optical reflectivity, photon absorption, penetration depth, electron diffusion to the surface, escape probability, etc. Only photons absorbed by the metal can lead to photoemission, and metals typically have high reflectivity.

4.3.1 Comparison to Theory

K. Jensen at the Naval Research Laboratory has recently developed a hard sphere model to account for the changes in workfunction and quantum efficiency of a surface as a function of the cesium coverage factor [30]. This development is considered an integral part of the overall photocathode research program and a collaborative effort coupling experimental results with theoretical prediction. The theory attempts to systematically reduce the large number of adjustable parameters by accounting for laser heating of the material, heat transport, photoemission, and surface conditions using fundamental considerations and relationships. This is in contrast to other similar theories which simplify the model and subsequent calculation by allowing certain parameters to vary until the theory fits the data [31],[32],[33].

The first iteration of this theory was used to predict the QE versus coverage relation for cesium on tungsten and is plotted (solid line) along with experimental data from this project in Figure 36. Because the covalent diameter of cesium is 5.2 Ångstroms, it was assumed that 100% coverage was achieved when the Inficon deposition meter registered this value for thickness. Furthermore, coverage is expressed in terms of the coverage factor theta, where $\theta = 1$ implies complete monolayer coverage. The close agreement of experimental QE values obtained in this experiment to the NRL theory is striking, especially because *no adjustable parameters were arbitrarily chosen to obtain agreement*.

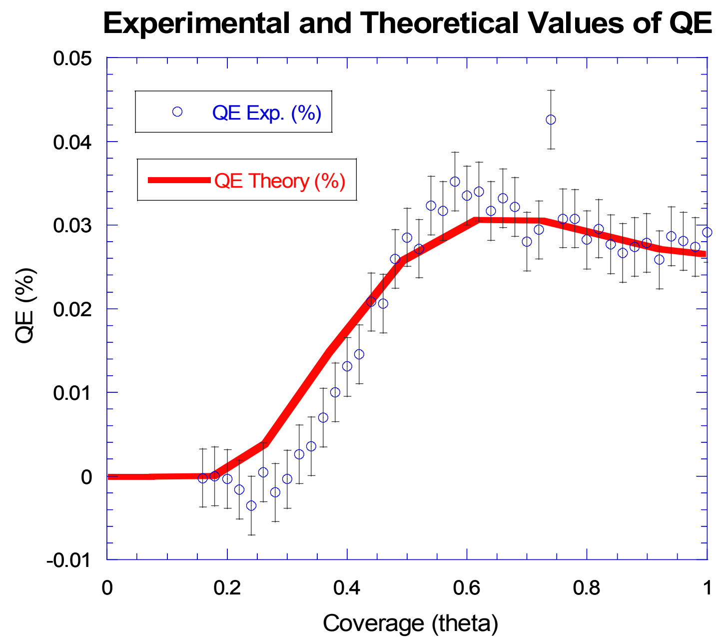

Figure 36: Comparison of QE - theory vs. experiment

All values used in the theoretical derivation are directly from the literature. This result serves both to validate the theory and motivate further investigation of cesium on other metals. It is clear that there is an optimum cesium coverage for which quantum efficiency is maximized, and that it is *less* than 100%. Jensen's theory predicts this by accounting for the changes in the effective dipole moment as a function of coverage factor [30]. The hard-sphere approach demonstrates the essential relation between coverage and dipole moment by considering the individual atomic radii of cesium and tungsten. Only a specific number of hard spheres of a given diameter can be geometrically arranged to create the largest possible dipole moment. When the number of adsorbed cesium atoms deviates significantly from this amount, the workfunction is increased because the electric field at the surface is reduced.

Based on the geometrical considerations mentioned above, the peak in quantum efficiency occurs at a sub-monolayer coverage of $\theta_m = 0.6$ which corresponds to approximately $3.20 \pm 0.05 \times 10^{14}$ atoms/cm^2 [29]. Using the rough approximation that one cesium atom occupies surface area $\pi R_{Cs}{}^2$ with $R = 2.6 \times 10^{-8}$ cm, a full monolayer coverage corresponds to $1/\pi R_{Cs}{}^2$ = 4.71×10^{14} atoms/cm^2 [34]. Thus, the surface density $3.20 \pm 0.05 \times 10^{14}$ atoms/cm^2 at which QE is optimized is given by

$$\theta_m = \frac{3.20 \times 10^{14}\,\text{atoms/cm}^2}{4.71 \times 10^{14}\,\text{atoms/cm}^2} = 0.68 \tag{1.14}$$

which closely agrees to the value of θ_m suggested by Figure 36. Because the NRL theory has so well predicted the behavior of the cesium on tungsten system, it is natural to test its application in other circumstances such as cesium on silver. This is, in fact, a next step in the research program and Figure 37 shows the predicted QE vs. coverage behavior that is expected experimentally using a blue 405nm laser.

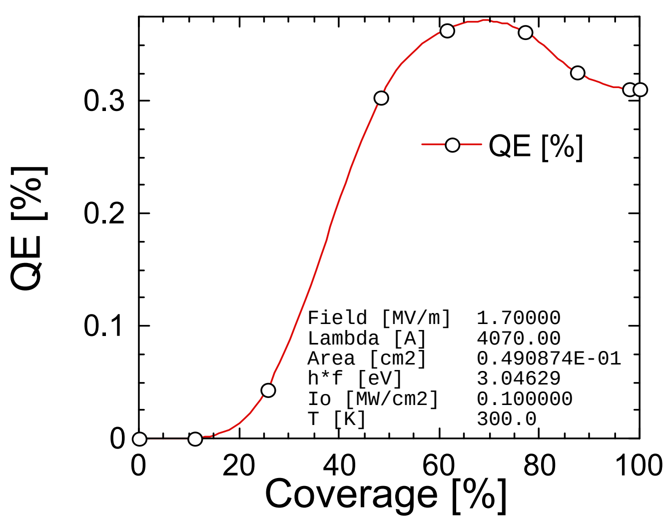

Figure 37: QE vs. coverage prediction for Cs-Ag [Jensen]

4.3.2 Relating QE to Surface Dynamics

Knowing the relationship between peak QE and cesium coverage allows further interpretation of the data provided by the plots in Figure 32. These plots show QE as a function of time as various thicknesses of cesium layers are evaporated from the surface. For thicknesses greater than a monolayer, a distinct peak in QE is observed and the time required to reach that peak increases as the film thickness increases. If initial cesium thickness is plotted as a function of the evaporation time required to reach optimal coverage, a near-linear relationship is observed, as shown in Figure 38.

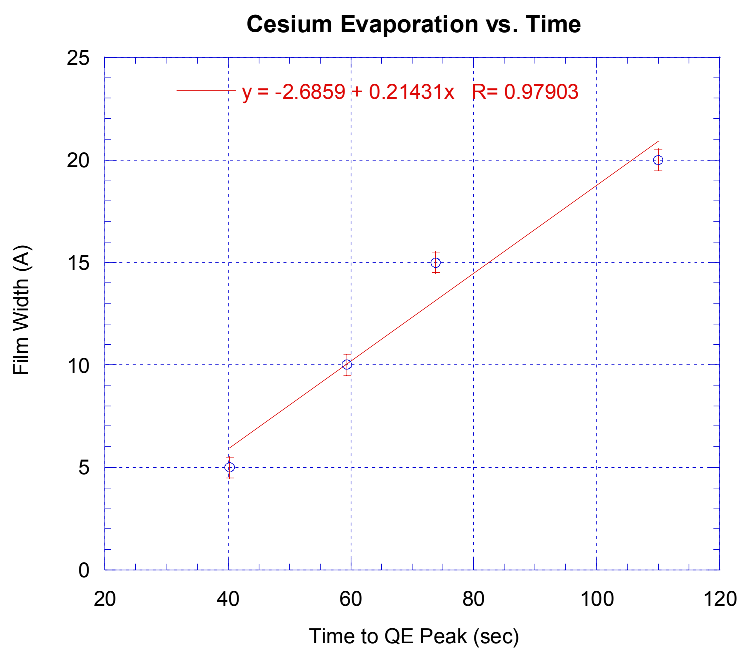

Figure 38: Evaporation bulk cesium vs. time

Because the films in Figure 32 (except for the first two) are all much thicker than one monolayer, the evaporation is that of bulk cesium. Because bulk cesium has a higher workfunction than cesiated tungsten, its QE will be lower [35]. This explains why QE starts low initially and rapidly increases as the bulk cesium evaporates down to a monolayer. The slope of Figure 38 is nothing other than the bulk evaporation rate of cesium, about 0.214 Ångstroms/sec. Given that the thickness of one monolayer is roughly twice the covalent radius of a cesium atom, this rate can be expressed as 0.04 monolayers/sec. Eventually, the optimum coverage θ_m is achieved and beyond this value, the QE begins to decrease again. The rate of change of QE is much slower in this regime, because the film is less than a monolayer thick and monolayer evaporation rates are lower than those of the bulk.

Following an analysis in the literature [34] on the evaporation of barium from dispenser cathodes, the bulk evaporation rate can be expressed using an Arrhenius relationship:

$$D_{bulk}(T) = D_0^{bulk} e^{\frac{-E_0^{bulk}}{k_B T}} \tag{1.15}$$

Knowing the average cathode temperature ($< 50^\circ\mathrm{C}$) and assuming published values of D_0^{bulk} for barium are also applicable to cesium, the thermal energy term can be calculated to be 1.042eV. This energy is lower than that of barium, whose thermal energy is $E_0^{Bulk} = 1.92987\mathrm{eV}$.

Chapter 5: Concluding Discussions

An important conclusion relative to future work is that the test chamber, evaporation techniques, vacuum procedures, and measurement methods yield repeatable experimental results that agree both with published literature and recent theory. The peak in QE at sub-monolayer coverage was seen in every evaporation run where more than one monolayer of cesium was initially deposited. The evaporation rates (monolayer and bulk) are in close agreement with that of a similar metal, barium. Most importantly, the QE vs. coverage behavior nearly identically mimics that predicted by Jensen. This agreement allows the use of that theory in predicting the behavior of more different (and eventually more complex) systems, including cesium on silver and multi-species dispenser photocathodes.

5.1 Future Work

Motivated by the close agreement between the NRL photoemission theory and the observed experimental behavior, the goal is now to systematically apply the theory to more complex situations. The first step will be to evaporate cesium onto other metals and compare with theoretical predictions. Eventually, compounds such as Cs_3Sb on tungsten will be tested and perhaps incorporated into the dispenser cathode concept.

5.1.1 Dispenser Cathode

The next major phase of this research involves testing of a recently fabricated dispenser cathode. A dispenser cathode contains an excess of cesium which can be selectively brought to the cathode surface as the existing layer evaporates and is damaged by contamination. This regeneration process may offer a way to overcome the limited lifetime associated with many higher QE cathodes. In the fabricating this particular dispenser cathode, a 5:1 mixture of titantium and cesium chromate powders was pressed into a capsule (about 1.5 grams) and placed into a small, stainless steel canister. A sintered tungsten disk 0.2mm thick was then laser-welded on the top. When heated in vacuum, it is expected that (at some activation temperature) the titanium powder will reduce cesium chromate to form titanium chromate and elemental cesium. The atomic cesium is smaller and can diffuse faster, so it should pass through the pores of the sintered tungsten to cover the surface through diffusion. This process of activating the cathode surface could occur *in situ* during a period of photoinjector downtime. Figure 39 shows a schematic diagram of a dispenser cathode and Figure 40 shows the one fabricated as part of this project.

Figure 39: Schematic of dispenser cathode

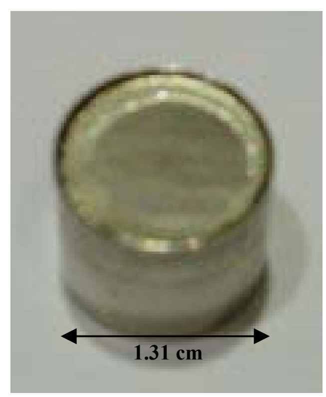

Figure 40: Fabricated dispenser cathode

The fabrication was performed by E-beam, Inc. and involved laser welding the tungsten disk to the stainless steel canister. The porosity of the sintered tungsten (pore size $\sim 1\mu\text{m}$) is demonstrated by pressurizing the canister with nitrogen and observing the gas bubble through a pool of ethanol situated on the surface, as shown in Figure 41.

A challenge in characterizing and understanding the behavior of a dispenser cathode is determining its activation temperature. By measuring photocurrent as a function of temperature, the results of this project (i.e. relating a peak value of QE to some sub-monolayer thickness of cesium) can be used to deduce the film thickness and evaporation rate.

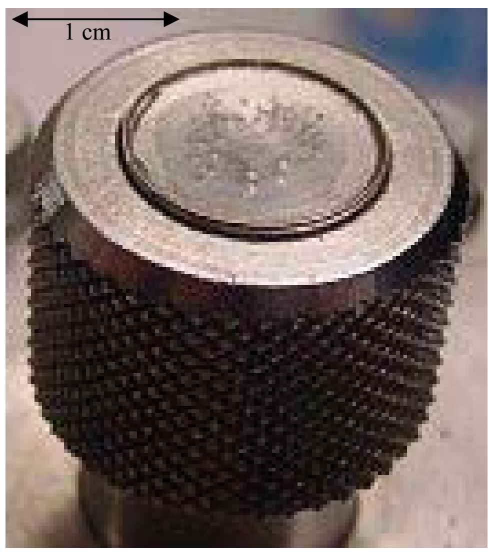

Figure 41: Porosity test of sintered tungsten disk

An obvious concern in refining the activation process is the fact that elevated temperatures accelerate cesium evaporation from the surface. For some length of time after activation, the cathode will remain hot and it is possible that the rejuvenated surface layer may evaporate significantly during the cool-down period. If this is indeed a problem, a way of cooling the cathode after rejuvenation may be necessary. Another practical issue will be pumping the system when the dispenser cathode is in place. Because the tungsten disk permits gas flow at a limited rate, there is a possibility that the canister would fracture from internal gas pressure if the chamber is evacuated rapidly, leaving trapped gas inside the dispenser. Residual gases in the cathode can be pumped much slower and will likely contribute to an elevated background pressure during operation. Despite these anticipated difficulties, however, the dispenser cathode offers an enormous advantage in lifetime extension by suggesting that a photosensitive surface can be rejuvenated *in situ* with little or no human intervention.

5.1.2 Lifetime Studies

It is unclear at this point to what degree duty factor plays in the time degradation of cathode performance. Duty factor is a measure of the extent to which a cathode is generating a photocurrent over a given period of time. The rough observation is that a cesiated tungsten cathode left to itself in a clean system will photoemit at near-peak capacity even after long periods of time. During continuous operation, however, there is clearly a time-dependent reduction in QE, due to contamination and evaporation. A definitive relationship between lifetime and duty factor is crucial in determining the frequency with which surface rehabilitation must occur.

5.1.3 Improving Photocurrent Accuracy

As seen in Figure 29, the photocurrents in this experiment include a large amount of digital noise introduced by the HP current meter (accuracy on the order of 10 nA). The meter's open-lead readings were graphed over time, and averaged to zero, so essential measurements could be made so long as the photocurrent was at least an order of magnitude larger than the noise. Such was the case for the blue laser, but photoemission from green was difficult to reliably measure because the signal to noise ratio was quite poor. A Keithley 486 picoammeter was recently purchased to introduce greater accuracy in the photocurrent measurement (and QE). It has resolution of 10fA, which should improve the accuracy of measurement by at least 4 orders of magnitude.

5.2 Summary and Conclusions

The purpose of this project was to characterize cesiated metal photocathodes in terms of quantum efficiency and lifetime and compare the results to theory recently developed at NRL. An experimental photocathode test facility was fabricated and equipped with data acquisition instrumentation. Tungsten was chosen as the cathode substrate because of its ability to be heated to high temperatures and because a large body of information exists concerning its surface interaction with electropositive materials. Photocathode fabrication involved evaporation of cesium onto a tungsten substrate and the resulting changes in workfunction were observed by measuring photocurrent.

A sub-monolayer thickness of cesium was observed to cause a peak in quantum efficiency. The results were obtained in two ways: 1.) starting with bare tungsten and measuring QE as cesium was slowly added, and 2.) starting with more than a monolayer thickness of cesium and slowly evaporating down to bare tungsten. Both methods showed in repeated experiments that QE peaks at 60-70% coverage, in very close agreement with Jensen's theory.

With strong experimental evidence that the theory accurately describes the photoemission process of cesiated metal cathodes, the next step is to predict and then test the behavior for other metals and surface compounds. Lifetime of higher QE cathodes is limited by surface evaporation and contamination. A scheme to rehabilitate the cesium surface layer has been devised and a prototype dispenser cathode was fabricated using sintered tungsten as a substrate. Upon activation, a sub-surface reservoir of cesium can diffuse to the surface and replenish the layer to restore cathode performance. If activation and surface diffusion processes can be sufficiently understood and refined, then the technology can be used to rejuvenate more complex cathodes that rely on the presence of cesium which deliver even higher quantum efficiency. The end goal is to fabricate a highly efficient, robust photocathode that can be operated in the visible range with a practical drive laser and for tractable lengths of time. After an inevitable amount of degraded performance, the cathode can be rehabilitated using the method above to restore optimum performance. Such a photocathode would be an ideal solution for many of today's accelerator applications.

Appendix: UHV System

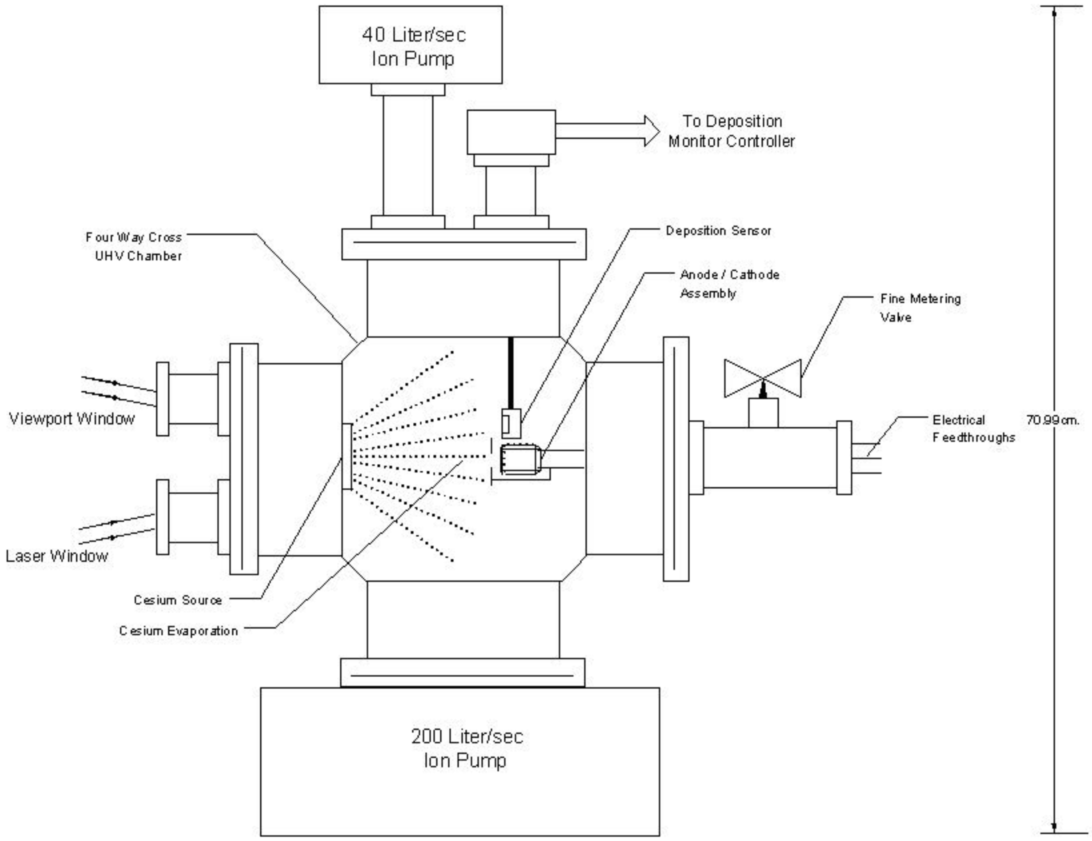

Figure 42: UHV system diagram

Bibliography

[1] A. H. Sommer and W. E. Spicer, “Photoelectric Emission,” chap. 4 in *Photoelectronic Materials and Devices*, Princeton, NJ: D. Van Nostrand Co., 1965.

[2] D. H. Dowell, S. Z. Bethel, K. D. Friddell, “Results from the average power laser experiment photocathode injector test,” *Nucl. Instr. and Meth. in Phys. Res.*, A 356 (1995) 167-176.

[3] P. G. O’Shea, et. al., “Performance of the Photoinjector accelerator for the Los Alamos Free-electron laser,” in *Proc. Particle Accel. Conf.*, vol. 5, San Fran., May 6–9, 1991, pp. 2754–2756.

[4] S. H. Kong, J. Kinross-Wright, D. C. Nguyen, R. L. Sheffield, “Photocathodes for free electron lasers,” *Nucl. Instr. and Meth. in Phys. Res.*, A 358 (1995) 272-275.

[5] K. Jensen, D. Feldman, N. Moody, et. al., “Thermal and field enhanced photoemission: comparison of theory to experiment.” (*submitted for publication*).

[6] H. Hertz, *Ann. Physik.*, vol. 31, p. 983, 1887.

[7] J. Elster, H. Geitel, *Ann. Physik.*, vol. 38, p. 497, 1889.

[8] L. R. Koller, “Photoelectric emission from thin films of cesium,” *Phys. Rev.* vol. 36, no. 11, Dec. 1930, pp. 1637-1647.

[9] N. R. Campbell, “The photoelectric emission of thin films,” *Phil. Mag. & Jour. of Sci.*, vol. 12, no. 173, July 1931, pp. 1814-1826.

[10] W. E. Spicer, A. Herrera-Gomez, “Modern theory and applications of photocathodes,” in *Proc. SPIE*, vol. 2022, San Diego, July 11-16, 1993, pp. 18-33.

[11] C. N. Berglund, W. E. Spicer, “Photoemission studies of copper and silver: experiment,” *Phys. Rev.* vol. 136, no. 4A, 16 November, 1964, pp. 1044-1064.

[12] A. L. Hughes and L. A. DuBridge, *Photoelectronic Phenomena*, New York, NY: McGraw-Hill, 1932.

[13] H. Frohlich, R. A. Sack, “Light Absorption and selective photo-effect in adsorbed layers,” *Proc. Phys. Soc.*, vol. 59, pp. 30-33, 1947.

[14] R. H. Fowler, “The analysis of photoelectric sensitivity curves for clean metals at various temperatures,” *Phys. Rev.* vol. 38, no. 1, July, 1931, pp. 45-56.

[15] A. H. Sommer, *Photoemissive Materials: Preparation, Properties, and Uses*, New York, NY: John Wiley & Sons, 1968.

[16] P. A. Anderson, “The contact difference of potential between tungsten and barium: the external work function of barium,” *Phys. Rev.* vol. 47, no. 12, June, 1935, pp. 958-964.

[17] K. L. Jensen, et. al., “Time dependent models of field-assisted photoemission,” in *Proc. Intl. Vac. Nano. Conf.*, Cambridge, Mass. July 11-16, 2004.

[18] K. C. Mishra, R. Garner, P. C. Schmidt, “Model of work function of tungsten cathodes with barium oxide coating,” *Jour. Appl. Phys.* vol. 95, no. 6, 15 March, 2004, pp. 3069-3074.

[19] K. H. Kingdon, I. Langmuir, “The removal of thorium from the surface of a thoriated tungsten filament by positive ion bombardment,” *Phys. Rev.* vol. 22, no. 2, August, 1923, pp. 148-160.

[20] T. J. Lee, B. H. Lott, B. J. Hopkins, *Brit. Jour. Appl. Phys.* vol. 1, ser. 2, 4 April, 1968, pp. 1241-1244.

[21] M. K. Sullivan, “A method for calculating pressure profiles in vacuum pipes,” Stanford Linear Accelerator Center, Internal Note AP 94-6 (1994).

[22] P. He, H. C. Hseuh, R. Todd, “Pressure distribution simulation for SNS ring vacuum,” in *Proc. Particle Accel. Conf.*, vol. 2, San Fran., May 12-16, 2003, pp. 791-793.

[23] V. Mecea, R. V. Bucur, “The use of RF voltage in quartz crystal microbalance measurements: application to nonmetallic films,” *Jour. of Phys. E: Sci. Instr.*, vol. 7, no. 5, May 1974, pp. 348-349.

[24] J. Kouptsidis, A. G. Mathewson, *Deutsches Elektronen Synchrotron Notkestrasse Report*, 76/49 (1976).

[25] H. Hartwig, J. Kouptsidis, *IEEE Trans. Nucl. Sci.*, vol. 24, no. 3, 1977, p. 1248.

[26] N. R. Dean, E. W. Hoyt, M. T. Palrang, B. G. Walker, “Glow discharge processing vs. bakeout for aluminum storage ring vacuum chambers,” *Jour. of Vac. Sci. Tech.*, vol. 15, no. 2, March 1978, pp. 758-760.

[27] S. Zhang, “Glow discharge cleaning for the Fermi Lab main injector,” Fermi-Lab Main Injector Notes, MI-069.

[28] C.-S. Wang, “High photoemission efficiency of submonolayer cesium-covered surfaces,” *Jour. Appl. Phys.* vol. 48, no. 4, April, 1977, pp. 1477-1479.

[29] J. B. Taylor, I. Langmuir, “The evaporation of atoms, ions, and electrons from cesium films on tungsten,” *Phys. Rev.* vol. 44, no. 6, 15 Sept., 1933, pp. 423-457.

[30] K. L. Jensen, D. W. Feldman, M. Virgo, P. G. O’Shea, “Measurement and analysis of thermal photoemission from a dispenser cathode,” *Phys. Rev. ST Accel. Beams*, vol. 6, no. 8, 1 Aug., 2003.

[31] J. P. Girardeau-Montaut, C. Girardeau-Montaut, “Theory of ultrashort nonlinear multiphoton photoelectric emission from metals,” *Phys. Rev. B,* vol. 51, no. 19, 15 May, 1995, pp. 13560-13567.

[32] C. Tomas, J. P. Girardeau-Montaut, et. al., “Dependence of photoemission efficiency on the pulsed laser cleaning of tungsten photocathodes, part 1: experimental,” *Appl. Phys. A,* vol. 64, Nov., 1997, pp. 467-471.

[33] E. P. Gyftopoulos, J. D. Levine, “Work function variation of metals coated by metallic films,” *Jour. Appl. Phys.* vol. 33, no. 1, January, 1962, pp. 67-73.

[34] K. L. Jensen, Y. Y. Lau, B. Levush, *IEEE Trans. Plasma Sci.*, vol. 28, no. 3, June 2000, pp. 772-781.

[35] J. M. Macaulay, I Brodie, C. A. Spindt, C. E. Holland, “Cesiated thin-film field-emission microcathode arrays,” *Appl. Phys. Lett.,* vol. 61, no. 8, 24 Aug., 1992, pp. 997-999.